The Astrophysical Journal Letters, 966:L33 (16pp), 2024 May 10 https://doi.org/10.3847/2041-8213/ad41b7

Detecting Population III Stars through Tidal Disruption Events in the Era of JWST and Roman

Rudrani Kar Chowdhury[1], Janet N. Y. Chang[1], Lixin Dai[1], and Priyamvada Natarajan[2,3,4]
[1] Department of Physics, The University of Hong Kong, Pokfulam Road, Hong Kong; rudrani@hku.hk, lixindai@hku.hk
[2] Department of Astronomy, Yale University, New Haven, CT 06511, USA
[3] Department of Physics, Yale University, New Haven, CT 06520, USA
[4] Black Hole Initiative at Harvard University, 20 Garden St., Cambridge MA, 02138, USA
Received 2024 January 23; revised 2024 April 8; accepted 2024 April 15; published 2024 May 8

Abstract

The first-generation metal-free stars, referred to as Population III (Pop III) stars, are believed to be the first objects to form out of the pristine gas in the very early Universe. Pop III stars have different structures from the current generation of stars and are important for generating heavy elements and shaping subsequent star formation. However, it is very challenging to directly detect Pop III stars given their high redshifts and short lifetimes. In this Letter, we propose a novel method for detecting Pop III stars through their tidal disruption events (TDEs) by massive black holes. We model the emission properties and calculate the expected rates for these unique TDEs in the early Universe at $z \sim 10$. We find that Pop III star TDEs have much higher mass fallback rates and longer evolution timescales compared to solar-type star TDEs in the local Universe, which enhances the feasibility of their detection, although a good survey strategy will be needed for categorizing these sources as transients. We further demonstrate that a large fraction of the flare emissions are redshifted to infrared wavelengths, which can be detected by the JWST and the Nancy Grace Roman Space Telescope (Roman). Last but not least, we find a promising Pop III star TDE detection rate of up to a few tens per year using Roman, based on our current understanding of the black hole mass function in the early Universe.

Unified Astronomy Thesaurus concepts: Tidal disruption (1696); Population III stars (1285)

1. Introduction

The first generation of stars are believed to have formed from the pristine gas a few hundred million years after the Big Bang. These metal-free stars are commonly referred to as Population III (Pop III) stars. Pop III stars are believed to form in collapsed dark matter minihalos with masses of around $10^6 M_\odot$ at $z \sim 15$–20 (Abel et al. 2002; Bromm et al. 2002; Yoshida et al. 2006). The initial mass function (IMF) of these short-lived Pop III stars is expected to be tilted to higher masses and hence they are likely more massive than the current generation of forming stars (Population I, or Pop I stars). While there is uncertainty at the present time regarding the Pop III IMF, their masses are believed to lie within the range of $30 M_\odot$–$300 M_\odot$. Pop III stars are expected to be key players in the early Universe and they are believed to be responsible for reionizing the intergalactic medium (IGM; Sokasian et al. 2004; Johnson et al. 2007; Kulkarni et al. 2014), and lifting the fog of the dark ages and jump-starting structure formation. Moreover, Pop III stars produce metals in their core and therefore play a crucial role in bridging the gap between the metal-free primordial gas and higher-metallicity Population II (or Pop II) and Population I (Pop I) stars by polluting the IGM through supernovae explosions (Chen et al. 2024). Hence, as metal polluters that shape subsequent generations of star formation, Pop III stars are an important population to detect directly as this will enable constraining their properties and better understanding the evolution of subsequent generations of stellar populations.

A plethora of numerical studies have been carried out to track the formation of Pop III stars in the first few billion years of the Universe (Abel et al. 2002; Bromm et al. 2009; Park et al. 2021a; Saad et al. 2022; Prole et al. 2023). In particular, recent studies show that Pop III stars do not form in isolation, and that typically multiple Pop III stars can form inside a single minihalo (Clark et al. 2011; Liu & Bromm 2020; Park et al. 2021b). While it is generally believed that the Pop III star formation rate peaks around $z \sim 10$ (Scannapieco et al. 2003; Jaacks et al. 2018), there has been speculation that they could continue forming at lower redshifts if pristine gas pockets are available in galaxies (Jimenez & Haiman 2006; Liu & Bromm 2020).

Direct observation of Pop III stars, however, turns out to be extremely challenging. So far, only a few Pop III–like candidate objects have been identified (Vanzella et al. 2020; Welch et al. 2022): detected through serendipitous gravitational lensing (Rydberg et al. 2013; Vikaeus et al. 2022b), in pair-instability supernovae (Hummel et al. 2012; Regős 2020), in gamma-ray bursts (de Souza et al. 2011; Mesler et al. 2014; Lazar & Bromm 2022), and in recently claimed detection with JWST Near Infrared Spectrograph (NIRSpec) observations (Wang et al. 2022a).

In this Letter, we propose and explore in detail a novel detection channel for Pop III stars motivated by the unfolding JWST observations and evidence for the possible existence of massive black holes (MBHs) formed via direct collapse of gas in place at these early epochs (Bogdán et al. 2023; Natarajan et al. 2024). Therefore, Pop III stars stand to be revealed via the observation of their tidal disruption by MBHs in early galaxies. Recent JWST observations in combination with Chandra X-ray observations have revealed and confirmed the presence of an accreting supermassive black hole (SMBH) in the source UHZ1 at $z \approx 10.1$, a mere 470 Myrs after the Big Bang

(Bogdán et al. 2023), that is consistent with formation via direct collapse of gas (e.g., Loeb & Rasio 1994; Begelman et al. 2006; Choi et al. 2013).

Tidal disruption events (TDEs) are produced whenever a star approaches a MBH and comes within the distance at which the tidal force of the black hole exceeds the self-gravity of the star. In such cases, the star will be destroyed by the tidal force, which in turn will produce a luminous tidal TDE (Rees 1988; Evans & Kochanek 1989). At the present time about 100 TDEs of Pop I stars in the local Universe have been observed (Gezari 2021), and these are typically associated with powerful emission observed in multiple wave bands including X-ray, ultraviolet (UV), optical, and radio (Auchettl et al. 2017; Alexander et al. 2020; Saxton et al. 2020; van Velzen et al. 2021).

In this Letter, we model the properties of Pop III star TDEs. As these first stars are expected to exist primarily in high-redshift galaxies, their optical and UV emission will be redshifted, rendering them detectable in infrared (IR) wavelengths. This study is extremely timely due to the recent launch and successful data stream from the JWST (Gardner et al. 2006) and planning underway for the soon to be launched Nancy Grace Roman Space Telescope (Roman; Spergel et al. 2015). JWST and Roman operate in IR bands, covering wavelength ranges of 600–28,000 nm and 480–2300 nm, respectively. With the high-resolution Near Infrared Camera (NIRCam) and NIRSpec along with the Mid-Infrared Instrument, JWST has already started to revolutionize our understanding of the first galaxies and early MBHs (e.g., Castellano et al. 2022; Atek et al. 2023; Bogdán et al. 2023; Yajima et al. 2023). On the other hand, the planned extremely large field of view (FOV) of Wide Field Instrument (WFI) on board Roman is designed to observe a vast area of the sky, making it possible to detect numerous faint objects simultaneously. One of the primary objectives of Roman is to shed light on the matter distribution over a large range of redshifts to understand the nature of dark matter and expansion history of the Universe. Both missions are hence expected to yield a large sample of extremely faint high-redshift sources.

Our Letter is structured as follows. In Section 2, we introduce the basic structure of Pop III stars, based on which we calculate the key TDE parameters. We also introduce the fiducial model used to calculate the emission properties of these Pop III TDEs. In Section 3, we present our main results, predictions for the intrinsic and the observed emission spectra, luminosities, and the light curves of Pop III star TDEs. We also calculate event rates and discuss the detection prospects for this new class of sources with JWST and Roman. We conclude with a summary of our key findings and implications of our results for unveiling the early Universe with these new probes in Section 4.

2. Modeling Population III Tidal Disruption Events

2.1. Mass–Radius Relation of Pop III Stars

We consider Pop III stars in the main-sequence stage. Massive Pop III stars are primarily radiation-pressure dominated, so their structures can be approximated using a polytropic model with an index of $\gamma = 4/3$ or $n = \frac{1}{\gamma - 1} = 3$ (Bromm et al. 2001b). Throughout this work, we use the mass–radius relationship of Pop III stars adopted from Bromm et al. (2001b):

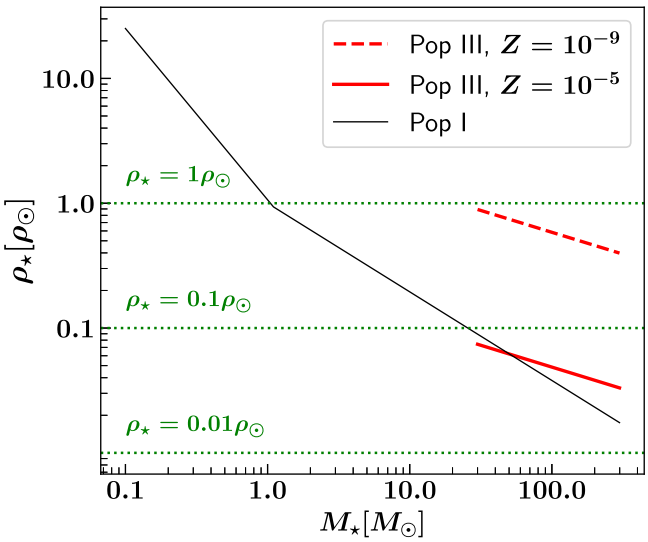

Figure 1. Average density ($\rho_\star$) of Pop III stars with $Z = 10^{-5}$ (red solid line) and $Z = 10^{-9}$ (red dashed line) in the mass range of 30–300$M_\odot$ compared to Pop I stars (black solid line) in the mass range of 0.1–300$M_\odot$. All stars are in their main-sequence stages. Pop III stars typically have $\rho_\star \sim 0.01$–$1\ \rho_\odot$ and those with lower metallicities or lower masses are denser. The stellar density of $1\rho_\odot$, $0.1\rho_\odot$, and $0.01\rho_\odot$ are marked with green dotted lines.

$$R_\star \simeq 0.7 R_\odot \left(\frac{M_\star}{M_\odot}\right)^{0.45} \left(\frac{Z}{10^{-9}}\right)^{0.09}, \quad (1)$$

where $M_\star$ is the stellar mass, $R_\star$ is the stellar radius, and Z is the metallicity of Pop III stars. When Z increases, cooling through metal lines is enhanced and the effective temperature of a Pop III star drops, which means the average stellar density also decreases given $\rho_\star \propto T^3$ for a polytropic star with $n = 3$ (Fowler & Hoyle 1964). Therefore, $R_\star$ increases with increasing Z. The value of the metallicity Z considered has varied from zero to a very small nonzero number in previous treatments (Bromm et al. 2001b; Schaerer 2003; Murphy et al. 2021; Klessen & Glover 2023). Many studies show that there likely exists a critical metallicity at which the transition from metal-free Pop III stars to metal-poor Population II (Pop II) stars occurs, and that value is $\sim 10^{-3}$–$10^{-5} Z_\odot$ depending on the IMF of Pop III stars (Bromm et al. 2001a; Schneider et al. 2002; Yoshida et al. 2004; Wise et al. 2012; Jaacks et al. 2018). Furthermore, Jaacks et al. (2018) show that the mean gas metallicity increases with decreasing redshift z and reaches $\sim 10^{-5} Z_\odot$ at $z \sim 10$. Hereafter, in this work in order to probe the metallicity dependence of our results, we calculate fiducial properties for Pop III stars with two chosen values for the metallicity: $Z = 10^{-5}$ and a lower metallicity of $Z = 10^{-9}$.

Given the stellar structure outlined above, we can calculate the average stellar density $\rho_\star$ of Pop III stars based on Equation (1). In Figure 1, we show the variation of $\rho_\star$ for Pop III stars as a function of their mass in the typical mass range of 30–300$M_\odot$ and compare that with the case of Pop I main-sequence stars. For the latter, we assume that their masses can extend to few hundreds of solar masses (Crowther et al. 2010; Rickard & Pauli 2023), and we adopt the mass–radius relation

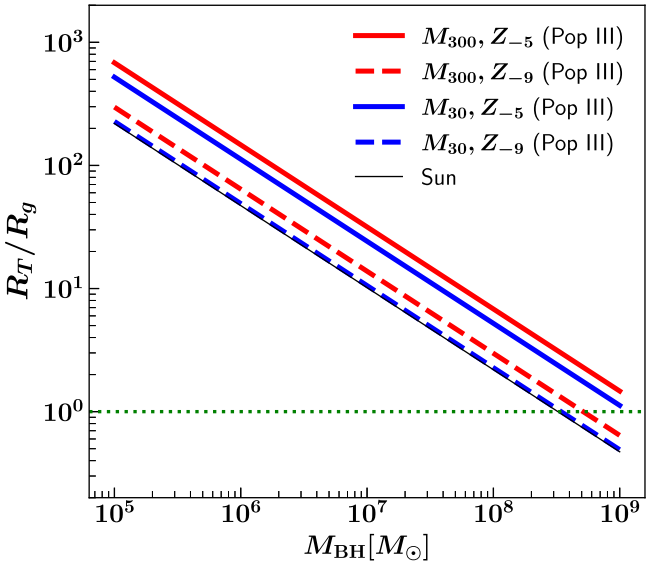

Figure 2. Tidal disruption radius R_T (scaled by the BH gravitational radius R_g) of Pop III stars and a solar-type star as a function of BH mass $M_{\rm BH}$. The red and blue solid or dashed lines represent Pop III stars of mass $300M_\odot$ (M_{300}) and $30M_\odot$ (M_{30}), respectively, with metallicity $Z = 10^{-5}$ (Z_{-5}) or 10^{-9} (Z_{-9}). The black solid line shows a solar-type star for comparison. It can be seen that a Pop III star, depending on its metallicity, has a R_T similar to or a few times larger than that of the Sun. The green dotted line indicates $R_T = R_g$, which gives the maximum mass of $M_{\rm BH}$ for a star to be disrupted inside the MBH event horizon.

from Kippenhahn & Weigert (1990):

$$R_\star \sim \begin{cases} R_\odot \left(\frac{M_\star}{M_\odot}\right)^{0.8}; & M_\star \leqslant 1M_\odot \\ R_\odot \left(\frac{M_\star}{M_\odot}\right)^{0.57}; & M_\star > 1M_\odot \end{cases}. \quad (2)$$

It can be seen that for both types of stars, $\rho_\star$ drops as the $M_\star$ increases. Furthermore, Pop III stars have $\rho_\star \sim \rho_\odot$ for the lower-metallicity case $Z \sim 10^{-9}$ and $\rho_\star \sim 0.1\rho_\odot$ as Z approaches the upper limit of 10^{-5}.

2.2. Tidal Disruption of Population III Stars

A star is tidally disrupted by a MBH when it approaches within its tidal disruption radius (R_T). To first order, R_T can be calculated using

$$R_T = R_\star \left(\frac{M_{\rm BH}}{M_\star}\right)^{1/3}, \quad (3)$$

where $M_{\rm BH}$ is the black hole (BH) mass. Therefore, for a fixed $M_{\rm BH}$, R_T only depends on the average stellar density ($R_T \propto \rho_\star^{-1/3}$). Figure 2 shows a comparison of R_T for Pop III stars (of different masses and metallicities) and with that for solar-type stars disrupted by MBHs with masses ranging from $M_{\rm BH} = 10^5$–$10^9 M_\odot$. It can be seen that the R_T for Pop III stars at very low metallicity ($Z \sim 10^{-9}$) are similar to that of the Sun, while the R_T for Pop III stars at relatively high metallicities ($Z \sim 10^{-5}$) are a few times larger, which is consistent with the density comparison seen in Figure 1.

Moreover, since $R_T \propto M_{\rm BH}^{1/3}$ while the gravitational radius of a BH $R_g \equiv GM_{\rm BH}/c^2 \propto M_{\rm BH}$, there exists a upper limit of $M_{\rm BH}$ (called the Hill mass) beyond which an approaching star is swallowed by the MBH as a whole. One can see in Figure 2 that the high-metallicity ($Z \sim 10^{-5}$) Pop III stars can be disrupted by MBHs with masses up to $10^9 M_\odot$. This can be used as an important indicator for Pop III TDE detection, since Pop I main-sequence stars can only be disrupted by MBHs with $M_{\rm BH} \lesssim 10^8 M_\odot$, except in the extreme case when the MBH has a close to maximal spin (Kesden 2012). Although the estimated mass of the BH in sources like UHZ1 (at $z \approx 10.1$) is estimated to be $\sim 4 \times 10^7 M_\odot$, it is expected that even more massive SMBHs could exist at these epochs, although they are expected to be extremely rare. Meanwhile, MBHs with masses less than that of UHZ1 could be significantly more numerous at these early epochs.

After the star is disrupted, about half of the stellar debris is ejected from the system and the rest remains bound to the MBH with a spread in its specific binding energy. The rate that the bound stellar debris orbits back to the pericenter is called the debris mass fallback rate ($\dot{M}_{\rm fb}$), which can be calculated as (Evans & Kochanek 1989; Phinney 1989)

$$\dot{M}_{\rm fb}(t) \approx \frac{1}{3}\frac{M_\star}{t_{\rm fb}}\left(\frac{t}{t_{\rm fb}}\right)^{-5/3}, \quad (4)$$

where the fallback time, $t_{\rm fb}$, is the orbital time of the most tightly bound debris.

In this work, we adopt the results from Guillochon & Ramirez-Ruiz (2013, hereafter GR13) who performed high-resolution hydrodynamical simulations to study this disruption process. In particular, adopting polytropic stellar models, GR13 provide the following fitting formulae for the debris fallback time and the peak mass fallback rate:

$$t_{\rm fb} = B_\gamma M_6^{1/2} m_\star^{-1} r_\star^{3/2} \ {\rm yr}, \quad (5)$$

$$\dot{M}_{\rm fb,peak} = A_\gamma M_6^{-1/2} m_\star^2 r_\star^{-3/2} \ M_\odot \ {\rm yr}^{-1}, \quad (6)$$

where $M_6 = M_{\rm BH}/10^6 M_\odot$, $m_\star = M_\star/M_\odot$, and $r_\star = R_\star/R_\odot$. Furthermore, for a polytropic star with $\gamma = 4/3$, the coefficients are as follows:

$$B_{4/3} = \frac{-0.38670 + 0.57291\sqrt{\beta} - 0.31231\beta}{1 - 1.2744\sqrt{\beta} - 0.90053\beta}, \quad (7)$$

$$A_{4/3} = \exp\left[\frac{27.261 - 27.516\beta + 3.8716\beta^2}{1 - 3.2605\beta - 1.3865\beta^2}\right]. \quad (8)$$

Here $\beta \equiv R_T/R_p$ is called the penetration factor, where R_p is the pericenter distance of the stellar orbit. A deep plunging orbit is commonly associated with $\beta \gg 1$, whereas mild or partial disruption is denoted by $\beta \sim 1$ and $\beta \lesssim 1$, respectively. GR13 showed that stars with polytropic index $\gamma = 4/3$ are fully disrupted when $\beta \gtrsim 1.85$, and under this condition $\dot{M}_{\rm fb,peak}$ remains similar. Hence, we mark this as the critical penetration factor β_c and use $\beta = \beta_c = 1.85$ for the calculations throughout this Letter unless otherwise specified. For $\beta = 1.85$, $B_{4/3} \sim 0.08$ and $A_{4/3} \sim 3$.

For Pop III stars, one can then use the mass–radius relationship (Equation (1)) and rewrite Equations (5) and (6) as

$$t_{\rm fb} \simeq 9\left(\frac{B_{4/3}}{0.08}\right)\left(\frac{m_\star}{300}\right)^{-0.3}\left(\frac{Z}{10^{-5}}\right)^{0.1} M_6^{0.5} \ {\rm day}, \quad (9)$$

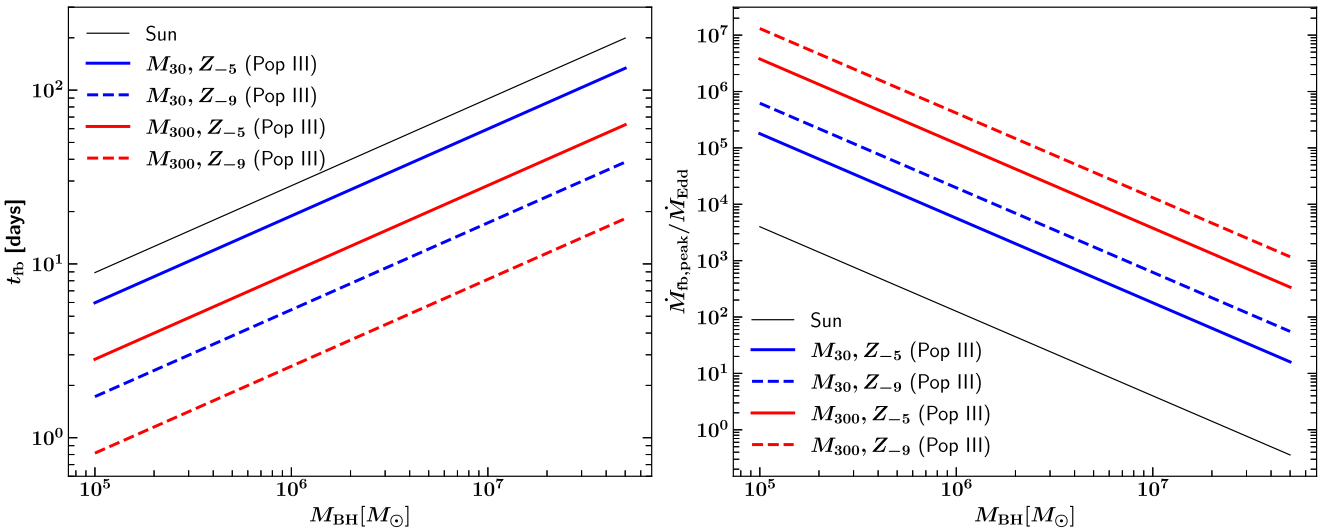

Figure 3. Left panel: debris mass fallback time $t_{\rm fb}$ for tidal disruption of $300M_\odot$ (M_{300}, red) and $30M_\odot$ (M_{30}, blue) Pop III stars with $Z = 10^{-5}$ (Z_{-5}, solid lines) and $Z = 10^{-9}$ (Z_{-9}, dashed lines) compared to a regular $1M_\odot$ star (black solid line). Right panel: Eddington ratio of the peak debris mass fallback rate $\dot{M}_{\rm fb,peak}$ for the same stars as in the left panel. Pop III stars have shorter fallback times and much higher peak mass fallback rates compared to Pop I star TDEs.

$$\dot{M}_{\rm fb,peak} \simeq 2.7 \times 10^3 \left(\frac{A_{4/3}}{3}\right)\left(\frac{m_\star}{300}\right)^{1.3}\left(\frac{Z}{10^{-5}}\right)^{-0.1} \times M_6^{-0.5}\, M_\odot\ {\rm yr}^{-1}. \quad (10)$$

We plot $t_{\rm fb}$ and $\dot{M}_{\rm fb,peak}$ as functions of $M_{\rm BH}$ for various Pop III stars compared to the Sun in Figure 3. It can be seen that $t_{\rm fb}$ for Pop III stars are usually around a few days, which is shorter compared to that of a solar-type star wherein $t_{\rm fb}$ ~a few tens of days for the case of $M_{\rm BH} = 10^6 M_\odot$. Furthermore, Pop III stars have extremely high $\dot{M}_{\rm fb,peak}$, which exceeds that of Pop I star TDEs by several orders of magnitude. For example, when $M_{\rm BH} = 10^6 M_\odot$, for Pop III star TDEs $\dot{M}_{\rm fb,peak}$ can reach $10^{4-6}\dot{M}_{\rm Edd}$, where $\dot{M}_{\rm Edd} \equiv L_{\rm Edd}/\eta c^2$ is the Eddington accretion rate of the black hole, with $L_{\rm Edd}$ being the Eddington luminosity, c the speed of light, and η the radiative efficiency with a nominal value of 0.1. This hyper-Eddington debris mass fallback rate is a consequence of the very large masses of Pop III stars coupled with their short debris mass fallback timescales.

After the peak of the flare, the debris mass fallback rate drops with time following $t^{-5/3}$. At late times, the fallback rate should transit from super-Eddington to sub-Eddington. We can calculate the timescale over which the fallback rate stays super-Eddington using $\dot{M}_{\rm fb} = \dot{M}_{\rm Edd}$:

$$t_{\rm Edd} \approx 38.5 \left(\frac{m_\star}{300}\right)^{3/5}\left(\frac{t_{\rm fb}}{10\ {\rm days}}\right)^{2/5} M_6^{-3/5}\ {\rm yr}. \quad (11)$$

This timescale is shown in Figure 4. It is clearly seen that Pop III TDEs have super-Eddington fallback rates for a much longer duration (up to hundreds of years) compared to a solar-type star TDE (a few years) considering $M_{\rm BH} = 10^6 M_\odot$.

We also note that there exist alternative models for the disruption process of stars. For example, a recent semi-analytical work by Bandopadhyay et al. (2024) showed that the fallback time could be almost independent of the stellar mass (in Pop I star TDEs). Yet these different models likely lead to consistent first-order results for the peak fallback rates, which matters the most for the observed flux (see Appendix A for comparison between models and more discussion).

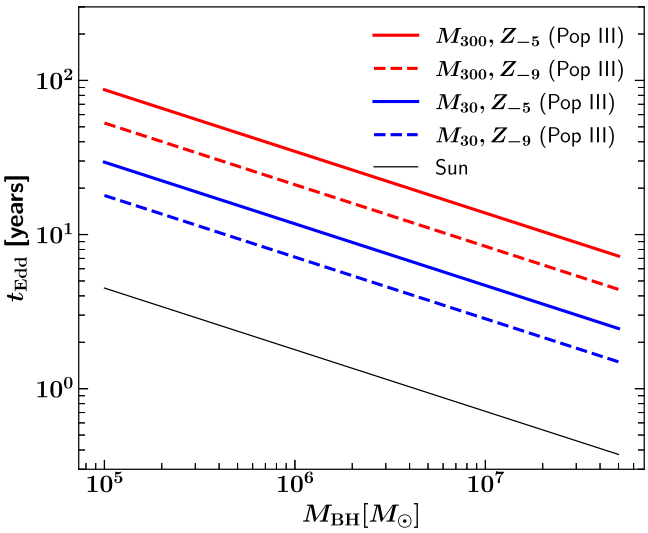

Figure 4. The Eddington timescale defined as the timescale that the debris mass fallback rate stays above the Eddington accretion rate. It is seen that Pop III star TDEs can stay super-Eddington for very long timescales (up to hundreds of years).

2.3. TDE Optical/UV Emission Model

The extremely high debris mass fallback rate seen in Figure 3 means that even if just a small fraction of the debris reaches the vicinity of the MBH, a super-Eddington accretion flow could result, which will launch powerful winds due to the large radiation pressure (Dai et al. 2018; Bu et al. 2023). Furthermore, outflows are also expected to be powered by debris stream collisions (Shiokawa et al. 2015; Bonnerot & Rossi 2019; Lu & Bonnerot 2020).

It has been proposed that these outflows are responsible for producing the optical/UV emission observed from TDEs in the local Universe (Loeb & Ulmer 1997; Strubbe & Quataert 2009; Lodato & Rossi 2011; Metzger & Stone 2016; Roth et al. 2016, 2020; Dai et al. 2021). There have also been sophisticated numerical simulations studying super-Eddington black hole accretion, outflow, and emission (Sadowski & Narayan 2016; Dai et al. 2018; Jiang et al. 2019; Thomsen et al.

2022). However, no simulation has been done yet to study super-Eddington accretion flows with Eddington ratios as high as 10^{5-7}. Given lack of guidance from simulations, we adopt an analytical model proposed by Strubbe & Quataert (2009, hereafter SQ09) to calculate the emission properties of Pop III star TDEs, while making a few changes to adapt model parameters consistent with more recent studies.

We first provide a brief summary of the SQ09 model below. SQ09 assume that during the early, super-Eddington phase a sizable fraction of the fallback material constitutes an outflow. Furthermore, they also assume that a fraction of the wind kinetic energy is converted to thermal energy, which in turn produces blackbody radiation. This assumption appears to hold even when the outflows are powered by debris stream collisions, and it is supported by recent simulations (Dai et al. 2018; Zanazzi & Ogilvie 2020; Andalman et al. 2022; Thomsen et al. 2022). SQ09 assume a spherical wind geometry and a constant wind velocity; under these circumstances, the wind density profile can be approximated as

$$\rho(r) = \begin{cases} \dot{M}_{\rm wind}/(4\pi r^2 v_{\rm wind}), & r \lesssim R_{\rm edge} \\ 0, & \text{outside} \end{cases}. \quad (12)$$

Here the wind mass rate $\dot{M}_{\rm wind}$ is assumed to be a constant fraction of the debris mass fallback rate so that $\dot{M}_{\rm out} \equiv f_{\rm out}\dot{M}_{\rm fb}$. We use a fiducial value $f_{\rm out} = 0.5$ (instead of $f_{\rm out} = 0.1$ used by SQ09), inspired by recent numerical simulations of super-Eddington accretion flows (e.g., Dai et al. 2018; Jiang et al. 2019; Thomsen et al. 2022). We recognize that the exact value of $f_{\rm out}$ has a dependence on the Eddington ratio, but our results do not significantly vary when $f_{\rm out} > 0.5$. $R_{\rm edge} \equiv v_{\rm wind}t$ denotes the edge of the wind. The wind velocity $v_{\rm wind}$ is assumed to be the escape velocity $v_{{\rm esc},L} \equiv \sqrt{2GM_{\rm BH}/R_L}$ at the wind-launching radius R_L, which is set to be $2R_p$ (the circularization radius). Therefore, we have $v_{{\rm esc},L} = \sqrt{GM_{\rm BH}/R_p}$, which can be further simplified as

$$v_{{\rm esc},L} = 0.1\beta^{1/2} m_\star^{1/6} r_\star^{-1/2} M_6^{1/3} c. \quad (13)$$

Furthermore, SQ09 calculate the temperature of the wind by assuming that the gas thermal energy density and kinetic energy density are similar at the wind-launching site:

$$aT_L^4 = \frac{1}{2}\rho_{{\rm fb},L} v_{{\rm esc},L}^2. \quad (14)$$

Here $a = \sigma/4$, with σ being the Stefan–Boltzmann constant, T_L the gas temperature at R_L, and $\rho_{{\rm fb},L}$ the gas density at R_L, which can be calculated as $\rho_{{\rm fb,L}} \equiv \dot{M}_{\rm fb}/(4\pi R_L^2 v_{{\rm esc},L})$. It is further assumed that the wind expands adiabatically so that its temperature scales with gas density:

$$T \propto \rho^{1/3}. \quad (15)$$

The photosphere radius of the wind, $R_{\rm ph}$, is located where

$$R_{\rm ph}\kappa_s \rho(R_{\rm ph}) \sim 1, \quad (16)$$

where κ_s is the electron scattering opacity, which is taken to be $0.35\,{\rm cm^2\ g^{-1}}$ assuming the hydrogen abundance for Pop III stars is ∼75%, while the rest of the mass is mostly dominated by helium (Bromm et al. 2009).

Initially, the wind gas density is very high due to the large fallback rate, so $R_{\rm edge}\kappa_s\rho(R_{\rm edge}) \gg 1$ and the photosphere almost coincides with the edge of the wind, which gives

$$R_{\rm ph} \approx R_{\rm edge} = 1.3 \times 10^3 f_v \beta^{1/2} m_\star^{1/6} r_\star^{-1/2} M_6^{-2/3} \left(\frac{t}{\rm day}\right) R_{\rm s}, \quad (17)$$

where $R_{\rm s}$ is the Schwarzschild radius of a nonspinning black hole. The effective temperature of the photosphere at this stage is given by

$$T_{\rm ph} \approx 1.5 \times 10^4 f_v^{-1/3} m_\star^{-7/72} r_\star^{1/24} M_6^{5/36} \times \left(\frac{t}{\rm day}\right)^{-7/36} \left(\frac{t_{\rm fb}}{\rm yr}\right)^{-1/18} {\rm K}. \quad (18)$$

As $R_{\rm edge}\kappa_s\rho(R_{\rm edge}) \propto \dot{M}_{\rm wind}/R_{\rm edge}$ decreases with t, after a certain time $R_{\rm edge}\kappa_s\rho(R_{\rm edge})$ drops to 1 and the photosphere starts to recede afterwards. This transition time is calculated to be

$$t_{\rm edge} \approx 9.6 f_{\rm out,0.5}^{3/8} f_v^{-3/4} B_\gamma^{1/4} M_6^{1/8} R_{p,3R_{\rm s}}^{3/8} m_\star^{1/8} r_\star^{3/8}\ {\rm day}, \quad (19)$$

where $f_{\rm out,0.5} \equiv f_{\rm out}/0.5$, and $f_v = v_{\rm wind}/v_{{\rm esc},L}$ (this fraction is set as 1 throughout this Letter unless otherwise specified). As we will show later, $t_{\rm edge}$ is also the time when the flare bolometric luminosity reaches the peak. We plot $t_{\rm edge}$ for Pop III stars and the Sun in Figure 5. It is clearly seen that the transition occurs on timescales of a few tens of days for Pop III stars as compared to a few days for the Sun in case of $M_{\rm BH} = 10^6 M_\odot$. This leads to larger photosphere radii and higher peak luminosities for Pop III TDEs.

After the photosphere starts to recede, the photosphere radius and temperature at this later stage can be estimated following Equations (15) and (16), and given as

$$R_{\rm ph} = \kappa_s \dot{M}_{\rm out}/(4\pi v_{\rm wind}) \approx 5.4 f_{\rm out,0.5} f_v^{-1} \left(\frac{\dot{M}_{\rm fb}}{\dot{M}_{\rm Edd}}\right) R_{p,3R_{\rm s}}^{1/2} R_{\rm s}, \quad (20)$$

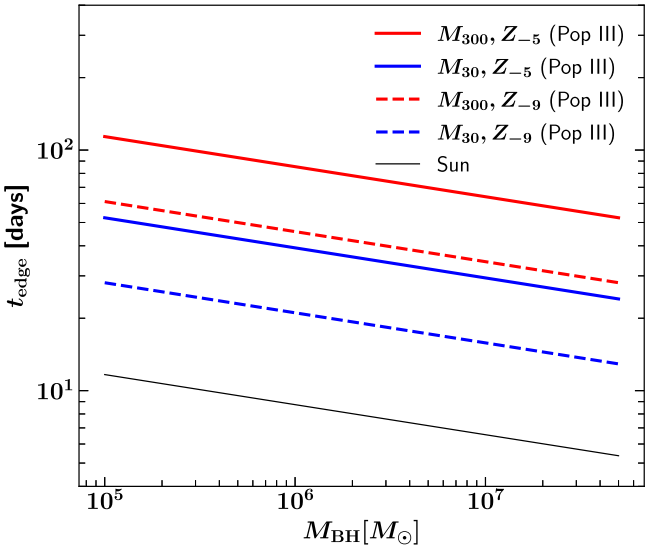

Figure 5. The time that the photosphere transits from expansion to recession ($t_{\rm edge}$) as a function of $M_{\rm BH}$ for various types of stars. The color scheme is the same as Figure 3. $t_{\rm edge}$ is longer for the Pop III stars compared to solar-type stars.

$$T_{\rm ph} \approx 2.5 \times 10^5 f_{\rm out,0.5}^{-1/3} f_v^{1/3} \left(\frac{\dot{M}_{\rm fb}}{\dot{M}_{\rm Edd}}\right)^{-5/12} M_6^{-1/4} R_{p,3R_s}^{-7/24} \ {\rm K}, \quad (21)$$

where $R_{p,3R_s} = R_p/3R_s$.

Specifically, for Pop III stars, using their mass–radius relationship (Equation (1)), we have

$$t_{\rm edge} \simeq 85 f_v^{-3/4} \left(\frac{f_{\rm out}}{0.5}\right)^{3/8} \left(\frac{B_\gamma}{0.08}\right)^{1/4} \left(\frac{\beta}{1.85}\right)^{-3/8} \times \left(\frac{m_\star}{300}\right)^{15/44} \left(\frac{Z}{10^{-5}}\right)^{3/44} M_6^{-1/8} \ {\rm day}. \quad (22)$$

Before $t_{\rm edge}$:

$$R_{\rm ph} \propto M_6^{1/3} m_\star^{-2/33} z_\star^{-1/22}, \quad (23)$$

$$T_{\rm ph} \propto M_6^{1/9} m_\star^{-2/33} z_\star^{-1/264}. \quad (24)$$

After $t_{\rm edge}$:

$$R_{\rm ph} \propto m_\star^{28/33} z_\star^{3/22}, \quad (25)$$

$$T_{\rm ph} \propto M_6^{2/9} m_\star^{-4/11} z_\star^{-17/264}. \quad (26)$$

We note that this first-order calculation in SQ09 assumes that the outflows start to be launched around the peak of the debris mass fallback rate and they ignore the outflows produced prior. The luminosity increases in the initial phase as the wind builds up, and therefore the characteristic rising time for the flare will be $t_{\rm edge}$ instead of $t_{\rm fb}$. While this assumption can cause issues for a solar-type star TDE which has $t_{\rm edge} \lesssim t_{\rm fb}$, it works well for Pop III star TDEs in which $t_{\rm edge} \gg t_{\rm fb}$. Therefore, Pop III star TDE flares should rise on timescales of $t_{\rm edge}$, i.e., a few weeks to months in the intrinsic TDE frame.

Furthermore, SQ09 also consider disk emission after the fallback rate drops to the sub-Eddington level. At this phase, the gas can radiate efficiently and a thin accretion disk is expected to form, which produces emission mainly in the X-ray and EUV bands. However, for Pop III star TDEs, as seen from Figure 4, the fallback rate stays super-Eddington for a very long time (tens to hundreds of years). Therefore, in this work we focus only on the emission produced from the winds launched in the super-Eddington phase and ignore the disk emission at very late times.

3. Results

3.1. Pop III Star TDE Intrinsic Emission Spectrum and Luminosity

We first calculate the TDE luminosity and spectral energy distribution (SED) in the rest frame of the host galaxy based on the properties of the photosphere described in Section 2.3. Assuming blackbody emission, the energy spectrum and bolometric luminosity can be computed using

$$\nu L_\nu = 4\pi^2 R_{\rm ph}^2 \nu B_\nu(T_{\rm ph}), \quad (27)$$

$$L = 4\pi\sigma R_{\rm ph}^2 T_{\rm ph}^4. \quad (28)$$

We plot the emission SEDs in Figure 6 and explore the dependence on various model parameters. The default set of parameters for a fiducial Pop III star TDE model is $M_{\rm BH} = 10^6 M_\odot$, $M_\star = 300 M_\odot$, $Z = 10^{-5}$, $f_{\rm out} = 0.5$, $f_v = 1$, and $\beta = \beta_c = 1.85$. We stick to these parameters for calculations unless specified otherwise.

We illustrate the evolution of the emission from a single TDE in Figure 6(a), which shows the SEDs at different epochs for the fiducial case. It is seen that initially the luminosity increases and the peak of the SED shifts slightly toward lower frequency as a result of increasing $R_{\rm ph}$ and decreasing $T_{\rm ph}$ during this phase. After $t_{\rm edge}$, $R_{\rm ph}$ recedes while $T_{\rm ph}$ increases, so the SED evolves in reverse, i.e., the luminosity decreases and the SED peak shifts toward higher frequency.

Figure 6(b) shows the SEDs at $t = t_{\rm edge}$ (the peak of the flare) from the TDEs of Pop III stars of different masses and metallicities in comparison to that of a solar-type star, all around a $10^6 M_\odot$ MBH. It can be immediately noticed that a significant fraction of the emission energy resides in the UV/optical wavelength regimes for all cases. The SEDs of Pop III star TDEs, compared to that of the solar-type TDE, have lower peak temperatures (with the SED peaking in the optical band instead of the UV) and slightly larger luminosities. However, the mass or metallicity of a Pop III star does not make a significant difference to its tidal flare emission. Increasing the metallicity leads to a slightly smaller luminosity and increasing the stellar mass shifts the SED toward slightly longer wavelengths.

Figure 6(c) shows the impact of $M_{\rm BH}$ on the SED. It can be seen that more massive black holes produce more luminous flares. Interestingly, the recent detection of sources such as UHZ1 (Bogdán et al. 2023) and GNz-11 (Maiolino et al. 2024) suggest that MBHs of $M_{\rm BH} \gtrsim 10^{6-7} M_\odot$ at $z \geqslant 10$ could be much more abundant than previously estimated. Therefore, it is likely that some Pop III TDEs can produce very luminous flares with intrinsic bolometric luminosity larger than 10^{45} erg s^{-1}.

Finally, Figure 6(d) shows how various other parameters, namely, $f_{\rm out}$ (outflow fraction), f_v (ratio between wind velocity and escape velocity), and β (stellar orbital penetration parameter), affect the SED. One can see that overall the choice of these parameters only mildly impacts the SED. We note that increasing $f_{\rm out}$ or decreasing f_v generally both lead to a larger peak luminosity. A lower β means the star is only partially disrupted, which will reduce the outflow mass, so the effect induced is similar to having a lower $f_{\rm out}$. Increasing β beyond β_c only slightly increases the peak fallback rate so it barely also affects the peak luminosity of the flare.

Next, we consider the evolution of the flare flux in specific wavelength bands. Figure 7 shows the optical (430–750 THz) and UV (750–3×10^4 THz) light curves of TDEs of Pop III and solar-type stars by a MBH of $M_{\rm BH} = 10^6 M_\odot$. For the fiducial Pop III star model, we also mark the epochs ($t = t_{\rm edge}/2$, $t_{\rm edge}$, $2t_{\rm edge}$, $4t_{\rm edge}$) on the light curves. One can see that both the optical and UV luminosities increase in the initial phase when $R_{\rm ph}$ traces the edge of the wind. However, the behavior of the UV and optical light curves after $t_{\rm edge}$ are different. For a solar-type star, since the peak of the flare SED stays in the UV regime, both the UV and the optical light curve reach the peak around $t_{\rm edge}$ and decay afterwards. However, for a Pop III star, the TDE flare SED shifts from UV to optical bands around $t_{\rm edge}$ and shifts back to the UV band afterwards. Therefore, while the tidal flare optical light curve still peaks at $t_{\rm edge}$, the UV light curve continues to rise for tens to few hundreds of days after $t_{\rm edge}$. Furthermore, at late times, while the optical luminosity decays rather closely following the debris mass fallback rate ($\propto t^{-5/3}$), the UV light curve has a

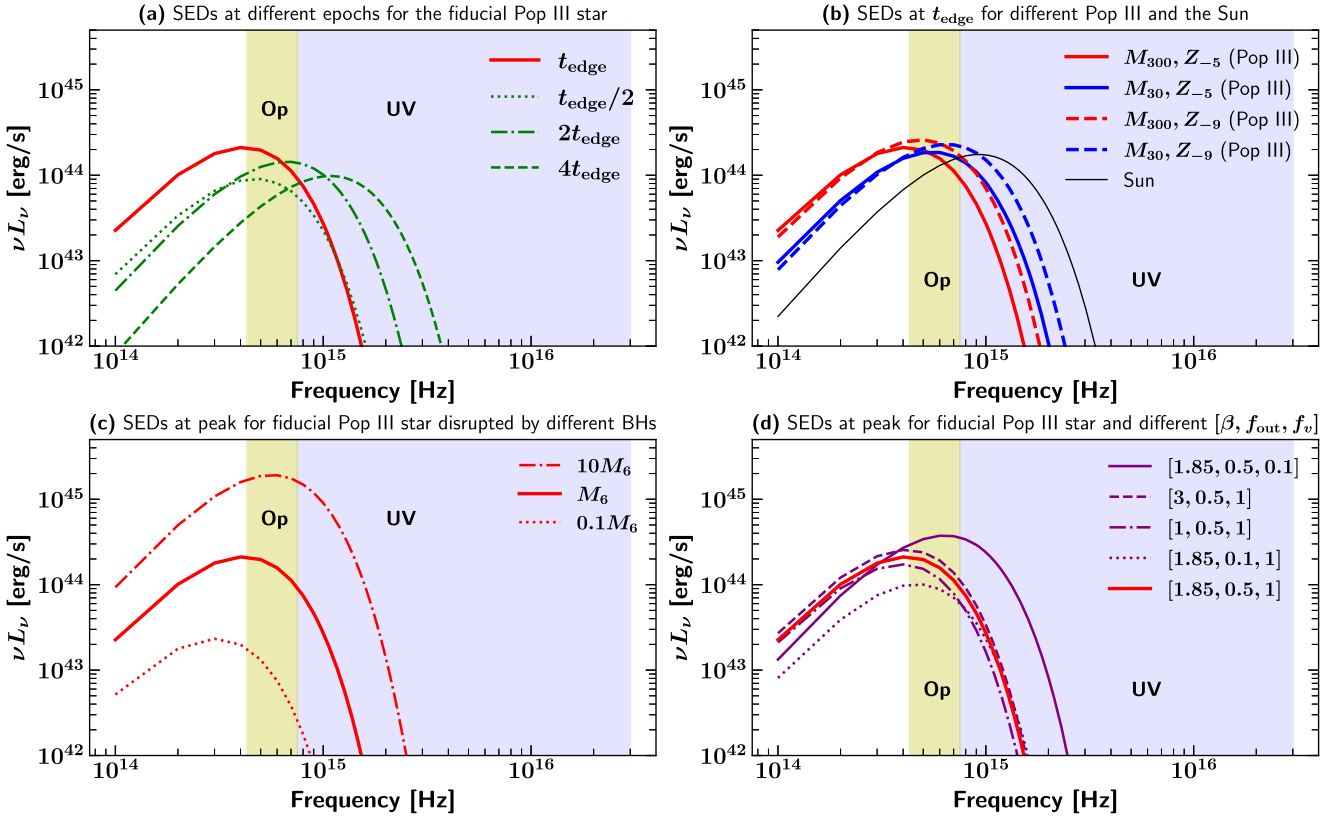

Figure 6. Spectral energy distributions (SEDs) of the Pop III star tidal flares in the rest frame of the host galaxy. The default parameter set used for plotting this figure and the those subsequent is $M_{\rm BH} = 10^6 M_\odot$, $M_\star = 300 M_\odot$ (M_{300}), $Z = 10^{-5}$(Z_{-5}), $f_{\rm out} = 0.5$, $f_v = 1$, and $\beta = \beta_c = 1.85$ (the red solid curve) unless specified otherwise. (a) The evolution of the SEDs at different epochs: $t_{\rm edge}/2$, $t_{\rm edge}$ (peak luminosity), $2\times$ $t_{\rm edge}$, and $4\times$ $t_{\rm edge}$. (b) The SEDs at $t = t_{\rm edge}$ for various Pop III stars of different masses or metallicities and a solar-type star. (c) The dependence of the SEDs (at $t = t_{\rm edge}$) on $M_{\rm BH}$. (d) The dependence of the SEDs (at $t = t_{\rm edge}$) on other parameters including the mass outflow fraction ($f_{\rm out}$), the ratio between wind velocity and escape velocity (f_v), and the stellar orbital penetration parameter β (with $\beta_c = 1.85$ being the critical value for full tidal disruption).

much shallower slope ($\propto t^{-0.57}$) due to the temperature evolution in this phase. This also means that the UV light curve has an evolution timescale longer than that of the optical light curve.

In summary, the bolometric luminosity of a Pop III star TDE in the rest frame of the host galaxy increases with a larger $M_{\rm BH}$, a smaller metallicity, a higher outflow fraction or a slower wind velocity, which all likely promote the potential observability of these TDEs. Furthermore, a higher Pop III mass will additionally serve to lengthen the evolution timescale of these light curves. We calculate the properties of the observed and redshifted TDE emission in the next section.

3.2. Pop III Star TDEs: Observed Fluxes and Light Curves

So far, we have established that the emission from Pop III TDEs mostly resides in UV/optical wave bands in the rest frame of the TDE host galaxy. In the subsequent calculations, we adopt a canonical value of redshift $z = 10$ for Pop III star TDEs and calculate the redshifted TDE emissions observed at $z = 0$.

With $\nu_{\rm e}$ and $\nu_{\rm o}$ denoting the rest-frame frequency and the observed frequency, respectively, the two are related as

$$\nu_{\rm e} = (1 + z)\nu_{\rm o}. \tag{29}$$

Therefore, the observed Pop III star TDE SED should be redshifted following $\nu_o = \nu_e/(1+z)$ and peaks around or slightly below 10^{14} Hz, which corresponds to $\lambda \sim 10^3$ nm. This means that a large fraction of the Pop III star TDE emission should be redshifted to the near-infrared (NIR) regime, and such events can be potentially detected by the NIRCam on JWST covering the wavelength range of 600–5000 nm as well as the WFI on Roman with a wave band of 480–2300 nm.

The observed specific flux, $F_\nu(\nu_{\rm o})$, is related to the rest-frame specific luminosity, $L_\nu(\nu_{\rm e})$, following (Hogg et al. 2002)

$$F_\nu(\nu_{\rm o}) = \frac{1+z}{4\pi D_L^2} L_\nu(\nu_{\rm e}). \tag{30}$$

Here D_L denotes the luminosity distance, which can be expressed as

$$D_L = (1 + z) D_c, \tag{31}$$

where

$$D_c = \frac{c}{H_0} \int_0^z \frac{dz}{\sqrt{\Omega_M (1+z)^3 + \Omega_\Lambda}}$$

is the comoving distance, and Ω_M, Ω_Λ, H_0 is the matter, energy density parameter, and Hubble constant at the current time, respectively.

We calculate the observed fluxes of Pop III TDEs at different epochs throughout the event for different stellar models using Equation (30). The results are plotted in Figure 8. It can be seen that for all models the fluxes in the NIR band stay above the detection limit of the JWST NIRCam (~11 nJy, corresponding

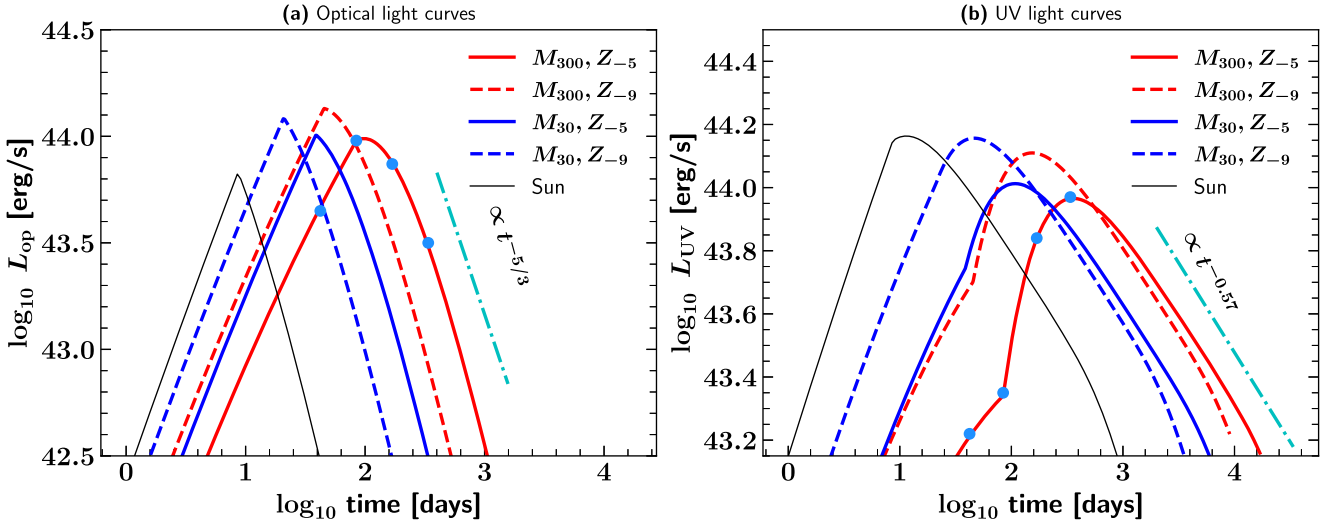

Figure 7. Optical (left) and UV (right) light curves of the Pop III star TDEs around a MBH with $M_{\rm BH} = 10^6 M_\odot$ in comparison to that that of a solar-type star. The color and line styles for different stars are the same as in Figure 3. For the fiducial Pop III star TDE model (the red solid curve), we mark the four epochs used in Figure 6(a) (i.e., $t_{\rm edge}/2$, $t_{\rm edge}$, $2\times t_{\rm edge}$, and $4\times t_{\rm edge}$) using light blue dots. The late-time light curves are fitted with power-law functions that are plotted using cyan dotted–dashed lines. We see that the Pop III star TDEs have much longer rise and decay timescales compared to standard TDEs of normal stars. Furthermore, for a Pop III star TDE, while its optical light curves follow the debris fallback rate relatively closely and peaks around $t_{\rm edge}$, its UV light curve peaks at a later time and decays much more slowly due to the temperature evolution of the flare.

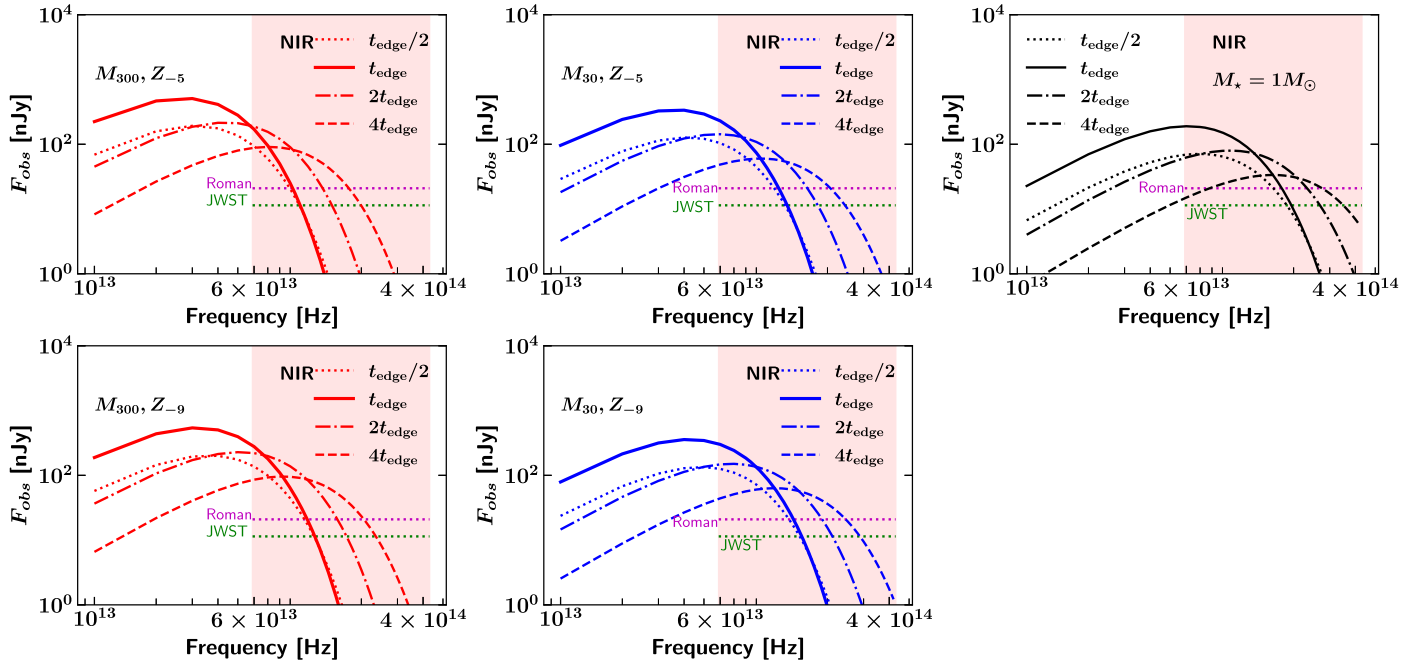

Figure 8. The observed fluxes of TDEs of Pop III stars of mass $300M_\odot$ (M_{300}, left panel) and $30M_\odot$ (M_{30}, middle panel) with different metallicities of 10^{-5} (Z_{-5}, top panel) and 10^{-9} (Z_{-9}, bottom panel) compared to a solar-type star (right panel) at different epochs ($t_{\rm edge}/2$, $t_{\rm edge}$, $2t_{\rm edge}$, $4t_{\rm edge}$). Green dotted line shows the sensitivity limit of the F150W filter of NIRCam. Magenta dotted line represents the sensitivity limit of the F106 filter of WFI, which has the best sensitivity limit of all the four filters (F106, F129, F158, F184) used in the High Latitude Wide Area Survey. Red shaded regions indicate JWST NIRcam bands. It can be seen that a large part of the fluxes are in the NIR wavelengths and lie above the detection limit of JWST's NIRCam and Roman's WFI.

to the F150W filter) and Roman WFI (∼20.9 nJy, corresponding to F106 filter) throughout these epochs. Also, no significant differences in the flux level are observed due to the different masses or metallicities of Pop III stars. Moreover, we note that the observed flux from the TDE of a disrupted solar-type star is also detectable by NIRcam and WFI.

Additionally, we have examined the dependence of observed flux on other model parameters, and the results are shown in Figure 9. Consistent with the results illustrated in Figures 6(c) and (d), one can see that the NIR flux increases significantly with increasing $M_{\rm BH}$ and moderately with decreasing f_v, but is barely affected by $f_{\rm out}$ and β. In particular, the NIR flux becomes undetectable even around peak luminosity when $M_{\rm BH} < 10^5 M_\odot$, unless the wind is exceptionally slow ($f_v \lesssim 0.1$). In summary, in all models, the observed Pop III star TDE NIR flux around flare peak stays significantly above the detection limit of NIRCam

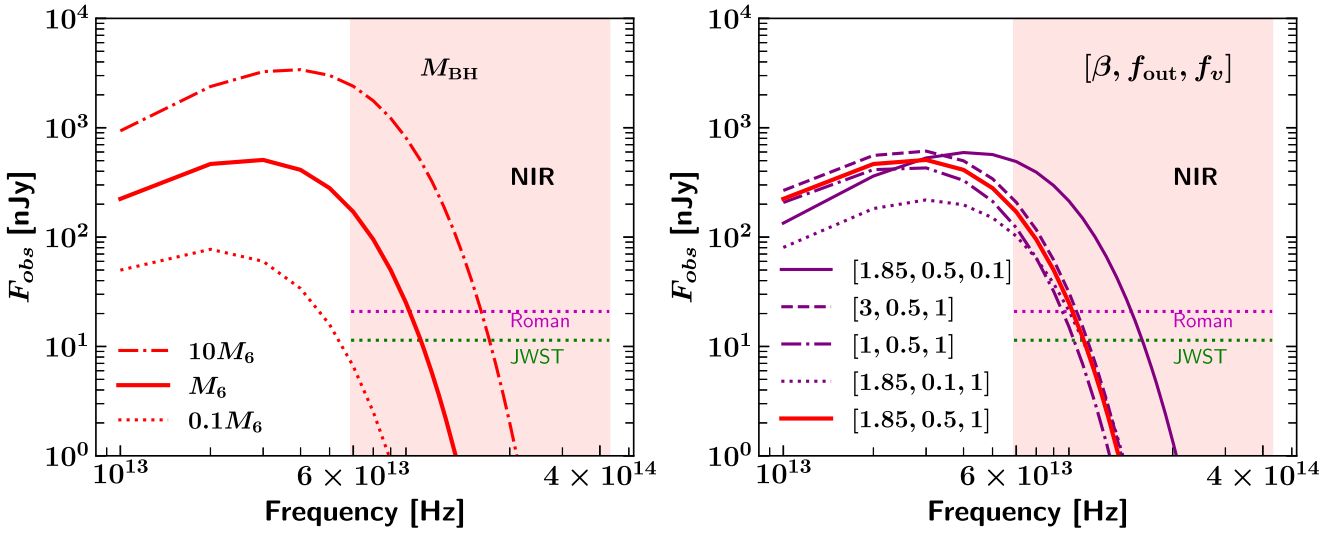

Figure 9. The dependence of the observed flux at $t = t_{\rm edge}$ on other parameters, such as the MBH mass ($M_{\rm BH}$), penetration factor (β), mass outflow fraction ($f_{\rm out}$), and wind velocity (f_v). Here we stick to the fiducial model of a Pop III star with $M_\star = 300 M_\odot$, $Z = 10^{-5}$. The shaded regions, magenta and green dotted lines are the same as in Figure 8.

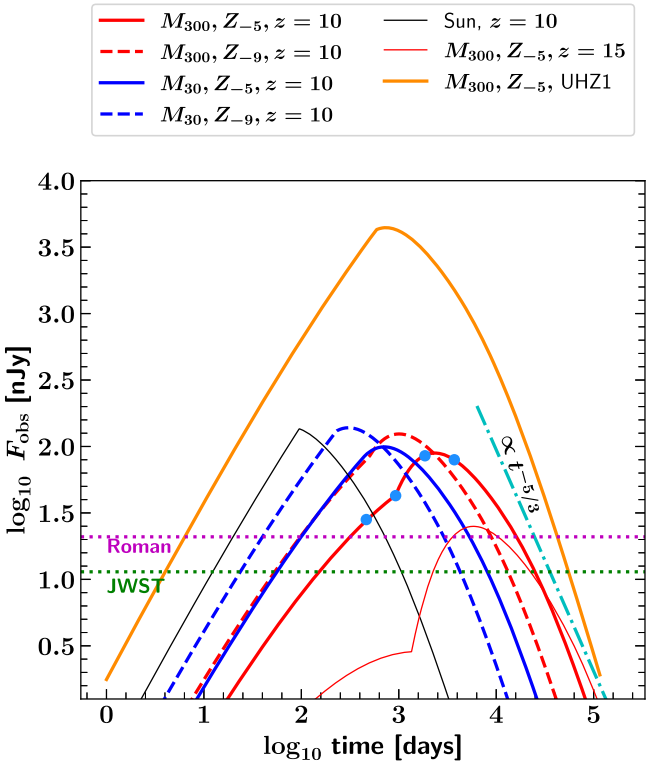

Figure 10. We show the NIR light curves of Pop III star TDEs in comparison to that of a solar-type star. The integrated NIR flux are in the JWST NIRcam band. All TDEs happen around a MBH with $M_{\rm BH} = 10^6 M_\odot$ at $z = 10$. Color schemes and line styles are the same as in Figure 7. Furthermore, for the default model of Pop III stars ($M_\star = 300 M_\odot = M_{300}$, $Z = 10^{-5} = Z_{-5}$), we also show the observed NIR light curve when the TDE happens at $z = 15$ (red thin line) or when the MBH is a UHZ1-like source with $M_{\rm BH} = 4 \times 10^7 M_\odot$ at $z = 10.1$ (orange line). The late-time light curves are compared to a power-law decay pattern of $t^{-5/3}$ (cyan dotted–dashed line). Green and magenta dotted solid lines denote the flux limit of NIRCam (F150W) and WFI (F106), respectively. It is noticed that the observed NIR light curves evolve very slowly due to cosmological time dilation.

and WFI, as long as $M_{\rm BH} \gtrsim 10^6 M_\odot$. Therefore, our results demonstrate that the detection of Pop III star TDEs at $z \sim 10$ with both JWST or Roman is feasible.

Next, we calculate the NIR light curves of Pop III star TDEs as would be observed in the JWST NIRcam band. The NIR light curves are shown in Figure 10, where one can see that the NIR flux can exceed both the JWST NIRCam and Roman WFI detection limits even when the TDE originates at $z = 15$. Moreover, at such high redshifts the time-dilation effect due to cosmological redshift is very strong, since $t_{\rm o} = (1+z) t_{\rm e}$. Taking a Pop III star TDE at $z = 10$ as an example, the observed NIR light curve (above the detection limit) rises on timescales $\sim$100–1000 days and decays over 10^3–10^4 days. At late time, the NIR flux still decays following a pattern relatively close to the classical mass fallback rate ($\propto t^{-5/3}$).

Furthermore, inspired by the recent discovery of UHZ1, we include the case of a Pop III star disrupted by a MBH with $M_{\rm BH} = 4 \times 10^7 M_\odot$ hosted by galaxy at $z = 10.1$ (orange line). As expected, the observed NIR flux is significantly higher in this case, which increases the chance of observing such events in current and upcoming NIR surveys.

Interestingly, given the observed Pop III star TDE flares rise over a few years, there is still a prospect of identifying such TDEs detected during the rising phase as transients, if multiple detections are made within the typical operation time of surveys. However, during the flare-decay phase, as the evolution timescale is very long these events will have almost near-constant brightness during the limited operation time, and therefore they are more likely to be miscategorized as active galactic nuclei (AGNs) based on their photometry. One promising method for distinguishing Pop III star TDEs from the TDEs of Pop I stars or AGNs is through spectroscopic follow-ups. Metal lines should be present in the spectra of either Pop I star TDEs or AGNs even at $z \sim 10$ given that gas is likely no longer metal-free (Yang et al. 2023). However, if a Pop III star TDE occurs in a previously quiescent galaxy, a metal-free spectrum should be produced, since all gas supplied to the MBH likely originates from the tidally disrupted Pop III star.

3.3. Rates of Pop III Star TDEs

We now estimate the intrinsic rates of Pop III TDEs in the early Universe. We adopt the approach in Pfister et al.

Table 1
Different IMFs of Pop III Stars Suggested by Different Works in the Literature

IMF	$\Phi(m_\star)$	α	m_c	Γ ($\mathrm{gal^{-1}\,yr^{-1}}$)	$\dot{N}_{\max}$ ($\mathrm{Mpc^{-3}\,yr^{-1}}$)
Greif et al. (2011)	$\propto m_\star^{-\alpha}$	−0.17	⋯	1.8×10^{-8}	1.1×10^{-9}
de Bennassuti et al. (2014)	$\propto m_\star^{\alpha-1}\exp(-m_c/m_\star)$	−1.35	$20M_\odot$	4.1×10^{-8}	2.5×10^{-9}
Jaacks et al. (2018)	$\propto m_\star^{-\alpha}\exp(-m_c^2/m_\star^2)$	0.17	$4.47M_\odot$	2.0×10^{-8}	1.2×10^{-9}

Notes. $\Phi(m_\star)$ describes the IMF equation, with α and m_c denoting the slope and cutoff mass, respectively. Γ represents the rate of Pop III star TDEs from a single galaxy with $M_{\rm BH}=10^6M_\odot$. $\dot{N}_{\max}$ represents the Pop III star TDE volumetric rate computed using the BHMF from the the merger-driven model.

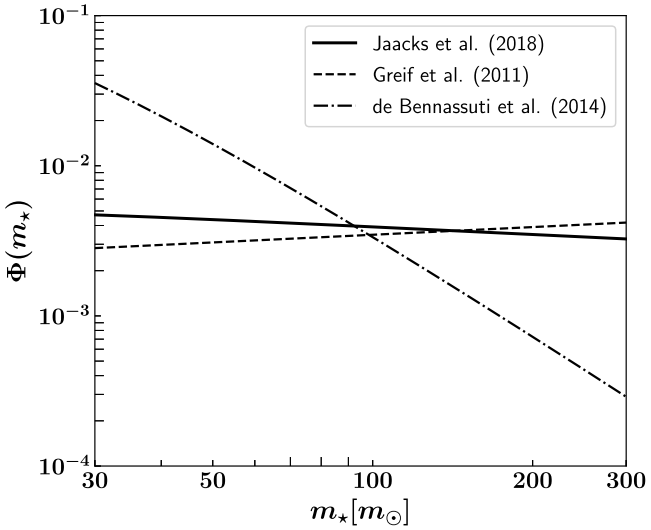

Figure 11. Different forms of IMF for the Pop III stars as listed in Table 1. It should be clarified that Jaacks et al. (2018) calculated Pop III IMF only within the mass range of $1M_\odot$–$150M_\odot$, and Greif et al. (2011) calculated the IMF only within the mass range of $0.1M_\odot$–$10M_\odot$. For this study, we extrapolated all three IMFs to the range of $30M_\odot$–$300M_\odot$.

(2020, 2022) to calculate the TDE rate through two-body scattering. The differential TDE rate is given by

$$\frac{d^2\Gamma}{d\log m_\star d\log\beta} = 8\pi^2 G M_{\rm BH}\frac{R_T}{\beta}\Phi(m_\star)m_\star \times\int_0^{E_m}\zeta(q,f,\beta,m_\star)\,dE. \quad (32)$$

Here $\Phi(m_\star)$ is the stellar IMF, E is the specific orbital energy of the star with the maximum value at $E_m=GM_{\rm BH}/R_T$ corresponding to the orbit with R_T as the closest approach, and $\zeta(q, f, \beta, m_\star)$ is a function of the loss-cone filling factor q, the stellar distribution function f, the stellar mass $m_\star$, and the penetration parameter β. The TDE of a Pop III star can be induced by the scattering between a Pop III star and a normal star or that between two Pop III stars. However, at the redshift range that we are considering, Pop III stars contribute to only a few percent of total stellar mass (Magg et al. 2022). Therefore, we only include the scattering of Pop III stars by normal stars into our calculation. Further details of the terms in Equation (32) and the rate calculation are given in Appendix B.

We summarize the assumptions used for the TDE rate calculation as below:

1. Ranges of parameters: we adopt a MBH mass range of $M_{\rm BH}=[10^5M_\odot,\ 10^8M_\odot]$, a Pop III stellar mass range of $m_\star=[30M_\odot,\ 300M_\odot]$, a normal star in the range of $m_\star=[0.1M_\odot,\ 10M_\odot]$, and a β in the range $[\beta_c=1.85, R_T/R_{\rm s}]$ to calculate the total TDE rate by integrating Equation (32).
2. IMF of the stellar populations: we adopt the general Kroupa IMF (Kroupa 2001) for the normal main-sequence stars. However, the IMF for Pop III stars is model dependent and not constrained very well yet. Different IMFs have been proposed in the literature, and a few examples are shown in Table 1 and Figure 11. However, using different Pop III star IMFs brings negligible effects to TDE rates, as explained in Appendix B.
3. Mass fraction of Pop III stars: Magg et al. (2022) showed that at $z\sim10$ Pop III stars have a mass fraction between 1% and 15% among the entire stellar population depending on the timescale at which Pop III stars transit to Pop II stars. We adopt a Pop III star mass fraction of 7% throughout the galaxy for our calculation.
4. Stellar density distribution: as there is a lack of studies of the structures of galaxies for different stellar populations at these extremely high redshifts, we follow classical papers such as those by Wang & Merritt (2004), Stone & Metzger (2016), and Pfister et al. (2020) and assume isothermal stellar density distributions in the Keplerian potential for both Pop III and normal stars, which gives
$$\rho(r)=\rho_0(r/r_{\rm inf})^{-\alpha}, \quad (33)$$
where $\rho(r)$ is the stellar density, $\alpha=2$, and $r_{\rm inf}=GM_{\rm BH}/2\sigma^2$, with σ being the velocity dispersion of the host galaxy.

Under these assumptions, the TDE rate of Pop III stars from a single galaxy hosting a $10^6M_\odot$ MBH is calculated and listed in Table 1. This intrinsic TDE rate is $\Gamma\sim10^{-8}\,\mathrm{gal^{-1}\,yr^{-1}}$, which is barely affected by the choice of Pop III star IMF.

One can further compute the volumetric rate of Pop III star TDEs using

$$\dot{N}=\iiint\frac{dn}{d\log M_{\rm BH}}\times\frac{d^2\Gamma}{d\log m_\star d\log\beta}\times d\log m_\star\, d\log\beta\ \ d\log M_{\rm BH}, \quad (34)$$

here $\Phi(M_{\rm BH})=dn/d\log M_{\rm BH}$ denotes the black hole mass function (BHMF), which is defined as the number of MBHs with masses between $\log M_{\rm BH}$ and $\log M_{\rm BH}+d\log M_{\rm BH}$ in unit comoving volume. We note that the BHMF at high redshifts sensitively depends on the seeding scenarios and growth channels of MBHs, much of which is currently uncertain. In this work, we adopt three different BHMFs from Trinca et al. (2022) that consider not only light, intermediate, and heavy MBH seeds but also different processes responsible for their growth. Figure 12 shows the BHMF at $z=10$ for these three

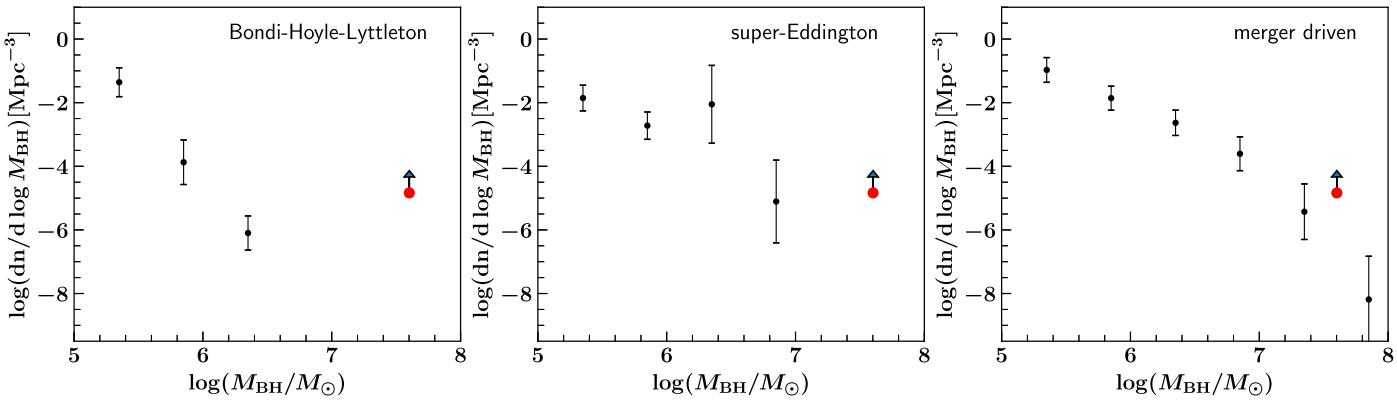

Figure 12. The black hole mass function at $z = 10$ for different growth models (left: Bondi–Hoyle–Lyttleton; middle: super-Eddington; right: merger driven). The BHMFs are adopted from Trinca et al. (2022) with permission. The red points in all three panels denote the BHMF inferred from the detection of UHZ1.

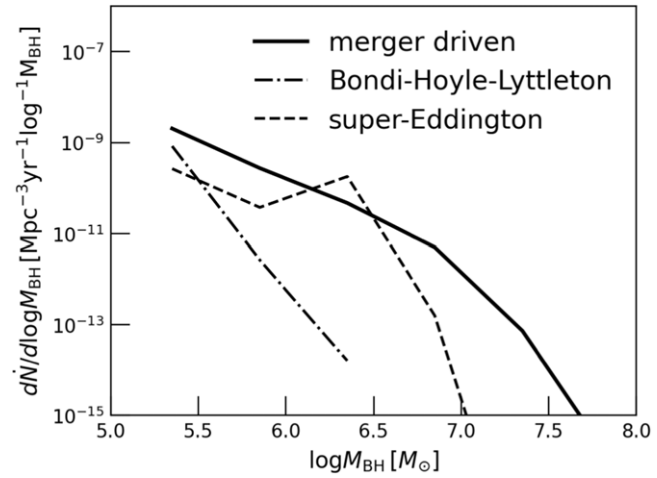

Figure 13. The differential Pop III star TDE volumetric rates as a function of M_{BH} for the three different BHMFs in Figure 12. One can see that the BHMF through the merger-driven growth channel overall produces the highest TDE volumetric rate.

growth models, namely, Eddington-limited Bondi–Hoyle–Lyttleton accretion, super-Eddington accretion, and merger-driven growth (Hoyle & Lyttleton 1941; Bondi 1952). We focus on the MBHs with $M_{BH} \geqslant 10^5 M_\odot$ for this work, since the observed Pop III star TDE flux goes below the threshold of NIRCam and WFI when $M_{BH} < 10^5 M_\odot$ (Figure 9). It is seen that the BHMF from the merger-driven growth channel generally has higher values in this M_{BH} range than the other two BHMF choices. The volumetric Pop III star TDE rates using these three different BHMFs are calculated and shown in Figure 13, which are around 10^{-10}–10^{-9} Mpc^{-3} yr^{-1}. Out of the three, not surprisingly, the BHMF based on the merger-driven growth model produces the highest integrated volumetric TDE rate $\dot{N}_{max} \approx 10^{-9}$ Mpc^{-3} yr^{-1}.

We also include the BHMF inferred from calibrating models with the detection of UHZ1 in Figure 12, and note that the BHMF taken from Trinca et al. (2022; as well as other current BHMF models) underestimates the number density of MBHs in all the growth models. Hence, it is possible that the actual Pop III TDE rate is higher than our estimate. An updated BHMF at high redshift from additional observations of a population of $z \sim 10$ black holes will be crucial for more accurately constraining the Pop III star TDE rate.

3.4. Pop III Star TDE Predictions for JWST and Roman

In this section, we estimate the total number of Pop III star TDEs that stand to be detected by the JWST and Roman telescopes. For a first-order estimate of the upper limit of the detection numbers, we ignore factors such as survey strategies and limitations. The total number can then be approximated using

$$N = \dot{N} \times V \times T. \tag{35}$$

Here $\dot{N}$ is the volumetric TDE rate obtained in the previous section, T is the duration of the observational survey, and V is the comoving volume from which the event can be detected. V can be computed using the following equation:

$$V = \frac{4\pi\,[d(z_{max})^3 - d(z_{min})^3]}{3} \times f_{sky}, \tag{36}$$

where $d(z)$ is the comoving distance dependent on redshift z, and f_{sky} is the sky coverage fraction of the telescope of survey.

For the case of Pop III star TDEs, we adopt $z_{min} = 10$ when the Pop III star population reaches peak, and $z_{max} = 15$ when both the Pop III stars and MBHs should have started to form. More importantly, we have predicted in Figure 10 that Pop III star TDEs at $z = 15$ are still bright enough to be detected by JWST and Roman. Moreover, for simplicity, we stick to a constant $\dot{N} = 1.2 \times 10^{-9}$ Mpc^{-3} yr^{-1} (based on the Pop III star IMF by Jaacks et al. 2018 and the BHMF from the merger-driven growth model), and note that this likely gives an upper limit to the detected number.

JWST Cycle 1 has various deep surveys, such as COSMOS-Web with a total area of 0.54 deg^2 and duration of 255 hr (Casey et al. 2023), and the JWST Advance Deep Extragalactic Survey (JADES) with its sky coverage of 236 arcmin^2 and a total duration of 426 hr considering both the deep and medium modes (Eisenstein et al. 2023). Using both the COSMOS-Web survey and the deep mode of the JADES survey, which can both probe galaxies at $z > 10$, the total detected number of Pop III TDEs in a year is about 5×10^{-4}. Throughout the 10 yr expected lifespan of JWST, even if we assume COSMOS-Web–like surveys are continuously conducted, the total expected detection number is still only $(10\,\mathrm{yr}/255\,\mathrm{hr}) \times 5 \times 10^{-4} \sim 0.2$ events in total. Therefore, the chance of detecting Pop III star TDEs using JWST is slim. If such TDEs were detected, it would indicate the BHMF at $z > 10$ is much larger than currently estimated, which would pose an interesting challenge in our understanding of the formation efficiency and evolution of MBHs in the early Universe. With the

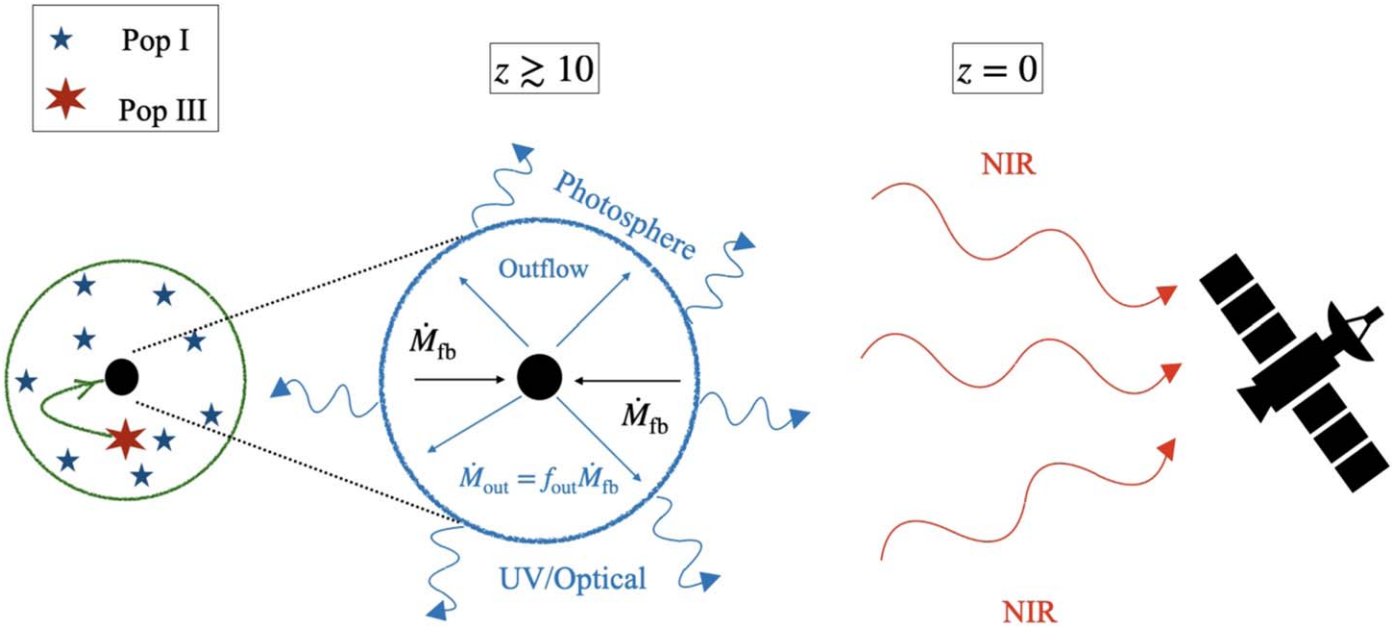

Figure 14. Schematic diagram of Pop III TDEs. In a galaxy at $z \gtrsim 10$, a Pop III star is scattered by other stars and gets tidally disrupted by the MBH. A large fraction of the fallback debris material is converted to a powerful wind with outflowing mass rate $\dot{M}_{\rm out} = f_{\rm out}\dot{M}_{\rm fb}$, which produces a luminous optical/UV flare. At $z = 0$, the flare emissions are redshifted to the NIR wavelength and can be detected by JWST and Roman.

recent discovery of UHZ1 and its interpretation as an OBG arising from a heavy initial seed by Natarajan et al. (2024), it appears that black hole seed formation in the early Universe can occur via multiple seeding pathways, hence rendering the process significantly more efficient than previously believed.

A much more promising telescope for detecting Pop III star TDEs is the upcoming Roman, which is designed to have a sensitivity similar to JWST (Figure 10) and to conduct wide-field surveys over a very large FOV of 0.281 deg^2 (Mosby et al. 2020). Hence, from the High Latitude Wide Area Roman survey, which aims to cover a total sky area of $\sim$2000 deg^2 (Wang et al. 2022b), the number of detected Pop III TDEs can reach $\lesssim$60 in a year. Furthermore, there is another proposed survey, the Next-generation All-sky Near-infrared Community surveY (or NANCY; Han et al. 2023), which plans to perform an all-sky scan. This survery strategy will lead to the detection of $\sim$1000 Pop III TDEs in a single year. Once a large sample of Pop III star TDEs has been observed, the number can be used to put a strong constraints on the properties and mass fraction of Pop III stars as well as the BHMF at $z \gtrsim 10$, which will provide the much needed insights into the efficiency of early black hole formation.

4. Summary and Discussion

Pop III stars are the first generation of stars, which are expected to have formed from metal-free primordial gas. Their formation and properties have been under study with multiple theoretical investigations, but their direct detection remains a challenging open question. The primary focus of this work has been to investigate the prospect of detecting Pop III stars through the flares produced when these stars are tidally disrupted by MBHs, utilizing telescopes such as JWST and Roman that can probe the high-redshift Universe. We summarize the key features of our assumed model and main findings below, and show a schematic illustration in Figure 14.

1. Pop III stars have tidal disruption radii around or a few times larger than that of a solar-type star. Very massive Pop III stars with $M_\star > 100 M_\odot$ can possibly be disrupted by MBHs with $M_{\rm BH}$ up to $\sim 10^9 M_\odot$.
2. The debris mass fallback rates for Pop III star TDEs can stay hyper-Eddington for long periods. For example, for a typical MBH with $M_{\rm BH} = 10^6 M_\odot$, $\dot{M}_{\rm fb}$ can reach a peak value of 10^4–$10^6 \dot{M}_{\rm Edd}$ and stays super-Eddington for 10–100 yr. In the more extreme case of a UHZ1-like source with $M_{\rm BH} \gtrsim 10^7 M_\odot$, $\dot{M}_{\rm fb,peak}$ drops to around 100–$10^5 \dot{M}_{\rm Edd}$ and $\dot{M}_{\rm fb}$ can still stay super-Eddington for more than a few years.
3. We adopt the super-Eddington outflow model proposed by SQ09 and only consider the emission produced by the outflow in this phase while predicting potential observational signatures.
4. In the rest frame of the host galaxy, Pop III star TDEs mainly produce UV/optical emission (Figure 6), with the bolometric luminosity increasing almost linearly with $M_{\rm BH}$. These tidal flares have much longer evolution timescales compared to typical Pop I star TDEs detected currently (Figure 7).
5. As Pop III star TDEs are expected to mostly occur at high redshifts ($z \gtrsim 10$), a large fraction of the emission is redshifted to the NIR band and the observed flux exceeds the detection limit of JWST NIRCam and Roman WFI (Figures 8 and 9). Moreover, due to the time-dilation effect, the observed NIR flares evolve even more slowly (rising in 100–1000 days and decaying over 10–100 yr; see Figure 10).
6. The volumetric rate of Pop III star TDEs is insensitive to the Pop III star IMF, but sensitively depends on the BHMF at high redshifts, which in turn depends on the seeding and growth models of MBHs.
7. We obtain an upper limit on the Pop III star TDE volumetric rate of $\sim 10^{-9}$ Mpc^{-3} yr^{-1} (Figure 13), based on the current BHMF model. We note that the recent

detection of overmassive black holes at high redshifts indicates that the density of MBHs at $z \sim 10$ and hence our estimated TDE rates could be lower than the actual numbers.

8. The high NIR luminosity and long duration of the Pop III star tidal flares make these events detectable by the Roman space telescope, and we predict up to a few tens of events per year with its wide-field instrument. However, the probability of detecting a Pop III TDE using JWST is low due to its narrower FOV.

Our results under the SQ09 model are rather robust against the choice of Pop III star mass, metallicity, and other model parameters such as the penetration parameter of the stellar orbit, outflow fraction and speed, etc. However, it should be acknowledged that several analytical models for TDE super-Eddington outflows have been proposed in the literature, which is mentioned in Appendix C. Also, very importantly, we note that this one-dimensional analytical model by SQ09 cannot explain the observed X-ray emissions produced in Pop I star TDEs in the local Universe. For the latter, simulations of super-Eddington disks around SMBHs with $\dot{M}_{\rm acc} \sim (1\text{–}10)\dot{M}_{\rm Edd}$ reveal that an optically thin funnel can form in the polar region through which X-rays can leak out (Dai et al. 2018; Jiang et al. 2019; Thomsen et al. 2022). However, it has been previously shown that the funnel can diminish when $\dot{M}_{\rm acc}$ reaches $>100\dot{M}_{\rm Edd}$ (Sadowski & Narayan 2016). Therefore, Pop III star TDEs with extremely high fallback rates likely cannot produce strong X-ray emissions, unless when relativistic jets are produced and pointing toward the observer. The production of jets under the context of super-Eddington accretion is still being actively explored (e.g., Coughlin & Begelman 2020; Ricarte et al. 2023), and the rates of jetted Pop III star TDEs can be used to probe the MBH spin distributiuon in the early Universe if the jet is magnetically driven (Blandford & Znajek 1977). Moreover, we note that the realistic structures of the massive stars can affect the TDE debris mass fallback rate calculation (Law-Smith et al. 2020). Therefore, future detailed modeling of Pop III star structures will be useful for improving our calculation.

As Pop III stars are short-lived, a fraction of them should have undergone substantial nuclear burning at the time of disruption and therefore have an evolved, more extended structure, which will increase the chance of the star being tidally stripped or partially disrupted. In this work, we have already calculated the impact of the penetration parameter on the TDE fluxes (Figure 6(d) and Figure 9). As expected, the debris mass peak fallback rate will be reduced in the case of partial TDEs, but the flare flux can still be detected by the JWST and Roman for moderate β values. Interestingly, recent studies have found that the rates of partial TDEs are significantly higher than the full disruption of solar-type stars in the local Universe (Zhong et al. 2022; Bortolas et al. 2023). The same could apply for Pop III star TDEs, which should greatly enhance their detection rates.

It is also worth mentioning that at the high redshifts we are considering, Pop III stars only occupy a few percent of the total stellar population, while Pop I and Pop II stars dominate the stellar mass and therefore should produce much higher TDE rates. Although the focus of this work is on Pop III star TDEs, we have shown that the NIR flux of Pop I star TDEs at $z \sim 10$ also exceeds the detection limit of JWST and Roman. Pop III star and Pop I star TDEs, however, can be distinguished by their different evolution timescales. Furthermore, the Population I star TDEs observed so far typically produce metal lines including C, N, O, Mg, and Fe lines in their optical or UV spectra (Blagorodnova et al. 2019; Leloudas et al. 2019; Gezari 2021; Charalampopoulos et al. 2022), and such signatures cannot be produced by Pop III star TDEs. Pop I and Pop II star TDEs at high redshifts are worth further investigation, which is beyond the scope of this Letter.

Another interesting aspect worth considering is the detection of TDEs at high redshifts magnified through gravitational lensing. Recent works show promising results of finding extremely faint high-z objects, including a number of Pop III star candidates, faint stars, distant galaxies, and black holes, with their observed fluxes largely boosted by nearby foreground lensing clusters (Kelly et al. 2018; Kaurov et al. 2019; Vikaeus et al. 2022a; Schauer et al. 2022; Bogdán et al. 2023; Diego et al. 2023; Meena et al. 2023; Chen et al. 2024; Szekerczes et al. 2024). Hence, the effect of lensing should also enhance the observed TDE fluxes, which will bring more high-z (Pop III) TDEs into view. While it has been shown that the chance of having a high-z galaxy lensed is roughly $\sim 10^{-3}$ (Saha et al. 2024), the probability of having lensed transients is yet to be studied in detail.

With the advent of JWST, the number of detected quasars with $M_{\rm BH} \gtrsim 10^9 M_\odot$ at $z > 6$ has increased by a large number (Wang et al. 2023; Yang et al. 2023; Natarajan et al. 2024), which offers interesting insights into the models of black hole seed formation. TDEs including Pop III TDEs could also be one of the channels responsible for the rapid growth of black hole seeds at very high redshifts. This was previously proposed by Pfister et al. (2021), who showed that intermediate-mass black holes at high redshifts can accumulate their masses through TDEs at a similar rate as through gas accretion.

In summary, in this work we compute the properties of a brand new class of high-redshift sources, tidally disrupted Pop III stars, and demonstrate that they could be viably detected in upcoming wide-field IR surveys. The prospect of observing such TDEs has only become promising due to the recent launch of JWST and the expected launch of Roman.

Acknowledgments

We thank A. Amruth, A. Bera, C. Bottrell, T. Kwan, S. Kimura, T. Matsumoto, L. Thomsen, N. Yoshida, and Z. Zhang for helpful discussions and A. Trinca for providing the data on BHMF. We also thank the referee for providing useful comments. R.K.C., N.Y.C., and L.D. acknowledge the support from the National Natural Science Foundation of China and the Hong Kong Research Grants Council (grant Nos. 12122309, N_HKU782/23, 17304821, 17314822, and 27305119). P.N. acknowledges support from the Gordon and Betty Moore Foundation and the John Templeton Foundation that fund the Black Hole Initiative (BHI) at Harvard University, where she serves as one of the PIs.

Appendix A
Comparison between Models for the Fallback Time and Peak Fallback Rate

In this work, we have followed the results obtained by GR13 to calculate the fallback time $t_{\rm fb}$ and peak fallback rate $\dot{M}_{\rm fb,peak}$ (Equations (5) and (6), respectively) in TDEs. GR13 used the hydrodynamical simulation FLASH to calculate these

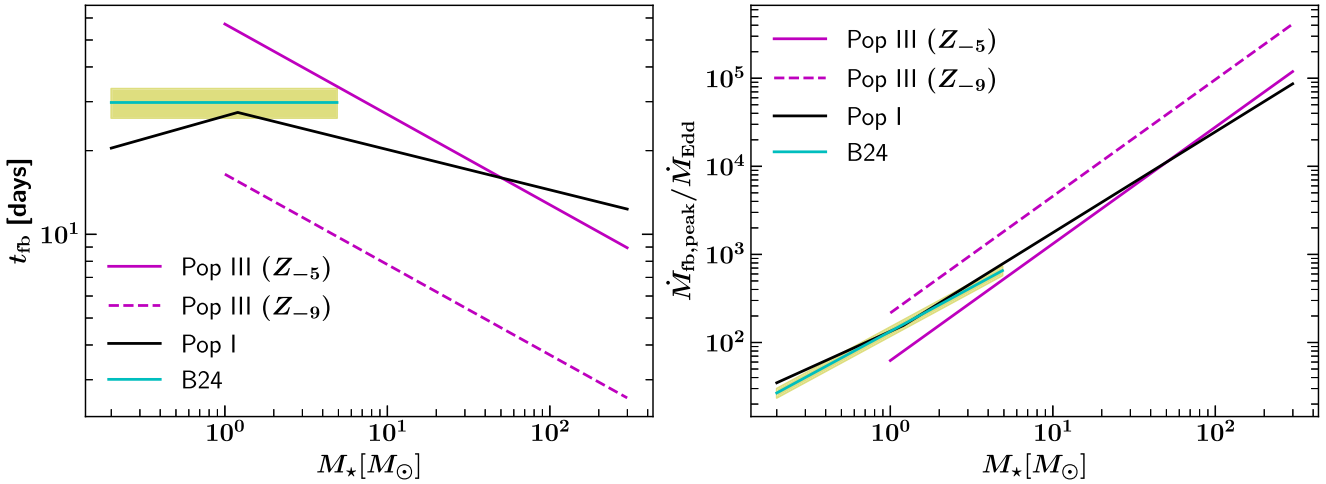

Figure A1. The fallback time $t_{\rm fb}$ and peak debris mass fallback rate $\dot{M}_{\rm fb,peak}$ as functions of stellar mass using both the GR13 model and the B24 model. The magenta solid and dashed lines represent the TDEs of Pop III stars with $Z = 10^{-5}$ and $Z = 10^{-9}$, respectively. The solid black line represents the TDE of Pop I stars. All of the lines mentioned above adopt the GR13 model. The cyan solid line represents the results from B24 for Pop I stars (in the stellar mass range of 0.2–5$M_\odot$). The yellow shaded regions denote the estimated uncertainties of the B24 model.

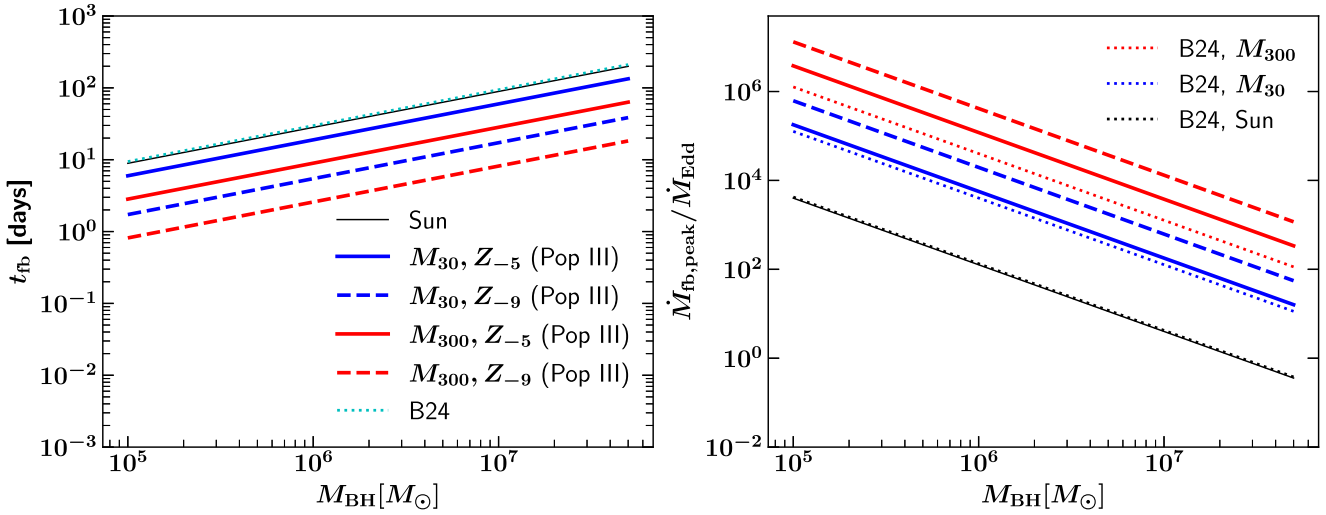

Figure A2. The fallback time $t_{\rm fb}$ and peak debris mass fallback rate $\dot{M}_{\rm fb,peak}$ as functions of the MBH mass using both the GR13 model and the B24 model. The solid and dashed lines are the same as Figure 3 (based on the GR13 model). The cyan dotted line in the left panel represents the fallback time using the B24 model. The black, blue, and red dotted lines in the right panel correspond to $\dot{M}_{\rm fb,peak}$ in the TDEs of a solar-type Pop I star, a 30$M_\odot$ Pop III star, and a 300$M_\odot$ Pop III star, respectively, using the B24 model.

parameters for different stellar structures assuming a polytropic density distribution with $\gamma = 4/3$ or $\gamma = 5/3$. There are a few recent works which have also investigated the disruption process and the dependence of $t_{\rm fb}$ and $\dot{M}_{\rm fb,peak}$ on stellar properties, such as mass and age, using simulations or semi-analytical calculations involving more accurate stellar structures obtained using MESA (e.g., Law-Smith et al. 2020; Coughlin & Nixon 2022; Bandopadhyay et al. 2024). Here we include a direct comparison on $t_{\rm fb}$ and $\dot{M}_{\rm fb,peak}$ between the GR13 model and the results from Bandopadhyay et al. (2024, hereafter B24).

We first plot the $t_{\rm fb}$ and $\dot{M}_{\rm fb,peak}$ as a function of the stellar mass $M_\star$ in Figure A1 for both Pop I and Pop III star TDEs. One can see B24 indicates that $t_{\rm fb}$ is independent of the stellar mass and structure, although their results were obtained by studying the TDEs of solar-metallicity stars in the mass range of 0.2–5$M_\odot$ only (and therefore we plotted the B24 result in this mass range). Also, for Pop I stars, the $\dot{M}_{\rm fb,peak}$ obtained by GR13 and B24 are quite similar (in the mass range of 0.2–5$M_\odot$).

We further plot $t_{\rm fb}$ and $\dot{M}_{\rm fb,peak}$ as a function of $M_{\rm BH}$ in Figure A2, which is the same as Figure 3 except that we have added additional curves based on the results of B24. Here if we assume the peak fallback rate formula in B24 would also apply for Pop III star TDEs, then the peak mass fallback rates do not deviate much from those calculated using the GR13 formula for stars with different masses and metallicities.

Appendix B
Calculation of TDE Rates

For a distribution of Pop III stars with a density profile following $\rho \propto r^{-\alpha}$ and a mass distribution expressed by $\Phi_{\rm PopIII}(m_\star)$, the TDE rate can be calculated using the loss-cone dynamics. We give a summary of the methodology as below and refer the readers to Pfister et al. (2020, 2022) for more details. The differential TDE rate can be expressed in

terms of stellar mass ($m_\star$), black hole mass ($M_{\rm BH}$), and the penetration parameter (β) such that

$$\frac{d^2\Gamma}{d\log m_\star d\log\beta} = 8\pi^2 G M_{\rm BH}\frac{R_T}{\beta^2}\Phi_{\rm Pop\ III}(m_\star)m_\star \times \int_0^{E_m}\zeta(q(E,m_\star),f(E),\beta,m_\star)dE. \quad \text{(B1)}$$

The specific binding energy E is integrated from 0 to the maximum energy $E_m = GM_{\rm BH}/R_T$. The function $\zeta(q, f, \beta, m_\star)$ is described as follows:

$$\zeta(q,f,\beta,m_\star) = \frac{f\log^2 e}{1+q^{-1}\xi(q)\ln(1/R_{\rm lc}(m_\star))} \times\left[1-2\sum_{m=1}^{\infty}\frac{e^{-\alpha_m^2 q/4}}{\alpha_m}\frac{J_0(\alpha_m\beta^{-1/2})}{J_1(\alpha_m)}\right], \quad \text{(B2)}$$

where $R_{\rm lc}$ describes the fraction of stars in the loss cone:

$$R_{\rm lc}(m_\star) = \frac{L_{\rm lc}^2}{L_{\rm circ}^2} \sim \frac{4ER_T(m_\star)}{GM_{\rm BH}}, \quad \text{(B3)}$$

and

$$\xi(q) = 1-4\sum_{m=1}^{\infty}\frac{e^{-\alpha_m^2 q/4}}{\alpha_m^2}. \quad \text{(B4)}$$

J_0 and J_1 are Bessel functions of the first kind, with general notation as

$$J_\alpha(x) = \sum_{m=0}^{\infty}\frac{(-1)^m}{m!\,\hat{\Gamma}(m+\alpha+1)}\left(\frac{x}{2}\right)^{2m+a}, \quad \text{(B5)}$$

where $\hat{\Gamma}(x)$ is the gamma function, and α_m is the mth zero of the Bessel function J_0.

If we assume the density follows an isothermal profile with $\alpha = 2$ (Equation (33)), the distribution function $f(E)$ takes an analytical form:

$$f(E) = (2\pi\sigma_{\rm inf}^2)^{-3/2}\frac{\rho_0}{\langle m_\star\rangle}\frac{\gamma(\alpha+1)}{\gamma(\alpha-1/2)}\left(\frac{E}{\sigma_{\rm inf}^2}\right)^{\alpha-3/2}, \quad \text{(B6)}$$

where $\sigma_{\rm inf} = (GM_{\rm BH}/r_{\rm inf})^{1/2}$ is the velocity distribution at the black hole influence radius $r_{\rm inf}$, $\langle m_\star\rangle$ is the average stellar mass of the Pop III stellar mass function $\Phi_{\rm PopIII}(m_\star)$, γ is the Euler gamma function, and ρ_0 is the central density:

$$\rho_0 = r_{\rm PopIII}\times M_{\rm BH}\frac{3-\alpha}{4\pi}\left(\frac{\sigma_{\rm inf}^2}{GM_{\rm BH}}\right)^3. \quad \text{(B7)}$$

Here $r_{\rm PopIII} = 0.07$ denotes the mass fraction of Pop III stars among all stellar populations in a galaxy at $z = 10$ (Magg et al. 2022). The loss-cone filling factor, q, can also be described as follows:

$$q(E,m_\star) = \nu(m_\star)\left(\frac{E}{\sigma_{\rm inf}^2}\right)^{\alpha-4}, \quad \text{(B8)}$$

with

$$\nu(m_\star) = \frac{8\sqrt{\pi}}{3}(3-\alpha)\frac{\gamma(\alpha+1)}{\gamma(\alpha-1/2)} \times\left[\frac{5}{32(\alpha-1/2)}+\frac{3I_B(1/2,\alpha)-I_B(3/2,\alpha)}{4\pi}\right] \times\left(\frac{G\langle m_{\rm scat}^2\rangle}{\sigma_{\rm inf}^2\langle m_\star\rangle R_T(m_\star)}\right)\ln\Lambda. \quad \text{(B9)}$$

Here $\ln\Lambda = \ln(0.4M_{\rm BH}/m_\star)$ is the Coulomb logarithm, $\langle m_\star\rangle = \int m_\star\Phi_{\rm PopIII}(m_\star)dm_\star$, and $m_{\rm scat}$ represents the total population of stars inside a galaxy that are available for scattering. To simplify the calculation, we assume all Pop III star TDEs are produced by the scattering between a Pop III star and a Pop I star, so that

$$\langle m_{\rm scat}^2\rangle = \int m_\star^2\Phi_{\rm norm}(m_\star)dm_\star. \quad \text{(B10)}$$

Furthermore, I_B is defined as

$$I_B\left(\frac{n}{2},\alpha\right) = \int_0^1 t^{-\frac{n+1}{2}}(1-t)^{3-\alpha}B\left(t,\frac{n}{2},\alpha-\frac{1}{2}\right)dt, \quad \text{(B11)}$$

with B as the incomplete Euler beta function.

As discussed in Section 3.3, the volumetric rate of a TDE is very mildly affected by the IMF of Pop III stars. This is mainly because that total TDE rate scales with $\langle m_{\rm scat}^2\rangle/\langle m_\star\rangle^2$, which does not differ much when the average is taken over the same mass range ($M_\star = 30M_\odot$–$300M_\odot$) for different IMFs.

Appendix C
Different TDE Outflow and Emission Models

In this work, we follow the TDE outflow and emission model proposed by SQ09. We note that there exist other models for the super-Eddington outflow properties in TDEs. Here we make a comparison with the ZEro-BeRnoulli Accretion (ZEBRA) flow model (Coughlin & Begelman 2014). In particular, we show the observed flux of a $300M_\odot$ Pop III TDE at $z = 10$ based on the ZEBRA model in Figure C1.

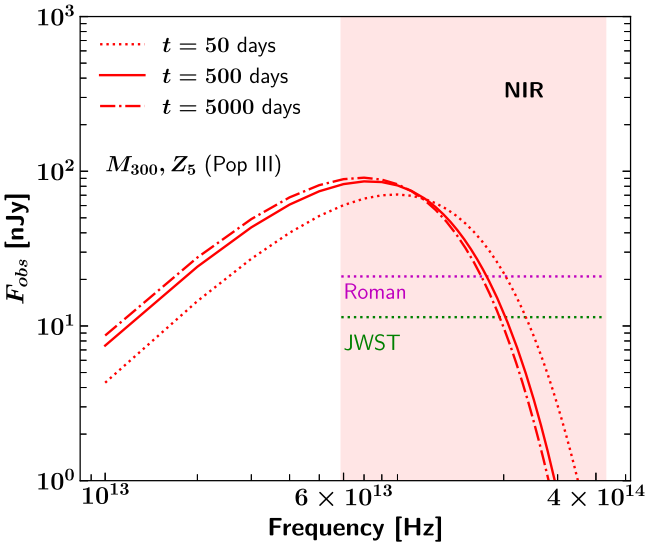

Figure C1. The observed flux of a Pop III TDE ($M_\star = 300M_\odot$, $Z = 10^{-5}$, $M_{\rm BH} = 10^6M_\odot$) at $z = 10$ using the ZEBRA model.

Comparing this with Figure 8 (top-left panel), one finds that both models produce a similar observed flux level. However, one can note that the SED peaks at slightly higher frequencies and evolves more slowly with time if adopting the ZEBRA model as compared to the SQ09 model.

ORCID iDs

Rudrani Kar Chowdhury https://orcid.org/0000-0003-2694-933X
Janet N. Y. Chang https://orcid.org/0009-0004-2575-1924
Lixin Dai https://orcid.org/0000-0002-9589-5235
Priyamvada Natarajan https://orcid.org/0000-0002-5554-8896

References

Abel, T., Bryan, G. L., & Norman, M. L. 2002, Sci, 295, 93
Alexander, K. D., van Velzen, S., Horesh, A., & Zauderer, B. A. 2020, SSRv, 216, 81
Andalman, Z. L., Liska, M. T. P., Tchekhovskoy, A., Coughlin, E. R., & Stone, N. 2022, MNRAS, 510, 1627
Atek, H., Chemerynska, I., Wang, B., et al. 2023, MNRAS, 524, 5486
Auchettl, K., Guillochon, J., & Ramirez-Ruiz, E. 2017, ApJ, 838, 149
Bandopadhyay, A., Fancher, J., Athian, A., et al. 2024, ApJL, 961, L2
Begelman, M. C., Volonteri, M., & Rees, M. J. 2006, MNRAS, 370, 289
Blagorodnova, N., Cenko, S. B., Kulkarni, S. R., et al. 2019, ApJ, 873, 92
Blandford, R. D., & Znajek, R. L. 1977, MNRAS, 179, 433
Bogdán, Á., Goulding, A. D., Natarajan, P., et al. 2023, NatAs, 8, 126
Bondi, H. 1952, MNRAS, 112, 195
Bonnerot, C., & Rossi, E. M. 2019, MNRAS, 484, 1301
Bortolas, E., Ryu, T., Broggi, L., & Sesana, A. 2023, MNRAS, 524, 3026
Bromm, V., Coppi, P. S., & Larson, R. B. 2002, ApJ, 564, 23
Bromm, V., Ferrara, A., Coppi, P. S., & Larson, R. B. 2001a, MNRAS, 328, 969
Bromm, V., Kudritzki, R. P., & Loeb, A. 2001b, ApJ, 552, 464
Bromm, V., Yoshida, N., Hernquist, L., & McKee, C. F. 2009, Natur, 459, 49
Bu, D.-F., Qiao, E., & Yang, X.-H. 2023, MNRAS, 523, 4136
Casey, C. M., Kartaltepe, J. S., Drakos, N. E., et al. 2023, ApJ, 954, 31
Castellano, M., Fontana, A., Treu, T., et al. 2022, ApJL, 938, L15
Charalampopoulos, P., Leloudas, G., Malesani, D. B., et al. 2022, A&A, 659, A34
Chen, K.-J., Tang, C.-Y., Ho, M.-Y., et al. 2024, ApJ, 964, 91
Chen, Z., Lu, Y., & Chen, Y. 2024, ApJ, 962, 3
Choi, J.-H., Shlosman, I., & Begelman, M. C. 2013, ApJ, 774, 149
Clark, P. C., Glover, S. C. O., Smith, R. J., et al. 2011, Sci, 331, 1040
Coughlin, E. R., & Begelman, M. C. 2014, ApJ, 781, 82
Coughlin, E. R., & Begelman, M. C. 2020, MNRAS, 499, 3158
Coughlin, E. R., & Nixon, C. J. 2022, MNRAS, 517, L26
Crowther, P. A., Schnurr, O., Hirschi, R., et al. 2010, MNRAS, 408, 731
Dai, J. L., Lodato, G., & Cheng, R. 2021, SSRv, 217, 12
Dai, L., McKinney, J. C., Roth, N., Ramirez-Ruiz, E., & Miller, M. C. 2018, ApJL, 859, L20
de Bennassuti, M., Schneider, R., Valiante, R., & Salvadori, S. 2014, MNRAS, 445, 3039
de Souza, R. S., Yoshida, N., & Ioka, K. 2011, A&A, 533, A32
Diego, J. M., Sun, B., Yan, H., et al. 2023, A&A, 679, A31
Eisenstein, D. J., Willott, C., Alberts, S., et al. 2023, arXiv:2306.02465
Evans, C. R., & Kochanek, C. S. 1989, ApJL, 346, L13
Fowler, W. A., & Hoyle, F. 1964, ApJS, 9, 201
Gardner, J. P., Mather, J. C., Clampin, M., et al. 2006, SSRv, 123, 485
Gezari, S. 2021, ARA&A, 59, 21
Greif, T. H., Springel, V., White, S. D. M., et al. 2011, ApJ, 737, 75
Guillochon, J., & Ramirez-Ruiz, E. 2013, ApJ, 767, 25
Han, J. J., Dey, A., Price-Whelan, A. M., et al. 2023, arXiv:2306.11784
Hogg, D. W., Baldry, I. K., Blanton, M. R., & Eisenstein, D. J. 2002, arXiv: astro-ph/0210394
Hoyle, F., & Lyttleton, R. A. 1941, MNRAS, 101, 227
Hummel, J. A., Pawlik, A. H., Milosavljević, M., & Bromm, V. 2012, ApJ, 755, 72
Jaacks, J., Thompson, R., Finkelstein, S. L., & Bromm, V. 2018, MNRAS, 475, 4396
Jiang, Y.-F., Stone, J. M., & Davis, S. W. 2019, ApJ, 880, 67
Jimenez, R., & Haiman, Z. 2006, Natur, 440, 501
Johnson, J. L., Greif, T. H., & Bromm, V. 2007, ApJ, 665, 85
Kaurov, A. A., Dai, L., Venumadhav, T., Miralda-Escudé, J., & Frye, B. 2019, ApJ, 880, 58
Kelly, P. L., Diego, J. M., Rodney, S., et al. 2018, NatAs, 2, 334
Kesden, M. 2012, PhRvD, 85, 024037
Kippenhahn, R., & Weigert, A. 1990, Stellar Structure and EvolutionVol. XVI (Heidelberg: Springer-Verlag)
Klessen, R. S., & Glover, S. C. O. 2023, ARA&A, 61, 65
Kroupa, P. 2001, MNRAS, 322, 231
Kulkarni, G., Hennawi, J. F., Rollinde, E., & Vangioni, E. 2014, ApJ, 787, 64
Law-Smith, J. A. P., Coulter, D. A., Guillochon, J., Mockler, B., & Ramirez-Ruiz, E. 2020, ApJ, 905, 141
Lazar, A., & Bromm, V. 2022, MNRAS, 511, 2505
Leloudas, G., Dai, L., Arcavi, I., et al. 2019, ApJ, 887, 218
Liu, B., & Bromm, V. 2020, MNRAS, 497, 2839
Lodato, G., & Rossi, E. M. 2011, MNRAS, 410, 359
Loeb, A., & Rasio, F. A. 1994, ApJ, 432, 52
Loeb, A., & Ulmer, A. 1997, ApJ, 489, 573
Lu, W., & Bonnerot, C. 2020, MNRAS, 492, 686
Magg, M., Reis, I., Fialkov, A., et al. 2022, MNRAS, 514, 4433
Maiolino, R., Scholtz, J., Witstok, J., et al. 2024, Natur, 627, 59
Meena, A. K., Zitrin, A., Jiménez-Teja, Y., et al. 2023, ApJL, 944, L6
Mesler, R. A., Whalen, D. J., Smidt, J., et al. 2014, ApJ, 787, 91
Metzger, B. D., & Stone, N. C. 2016, MNRAS, 461, 948
Mosby, G., Rauscher, B. J., Bennett, C., et al. 2020, JATIS, 6, 046001
Murphy, L. J., Groh, J. H., Farrell, E., et al. 2021, MNRAS, 506, 5731
Natarajan, P., Pacucci, F., Ricarte, A., et al. 2024, ApJL, 960, L1
Park, J., Ricotti, M., & Sugimura, K. 2021a, MNRAS, 508, 6176
Park, J., Ricotti, M., & Sugimura, K. 2021b, MNRAS, 508, 6193
Pfister, H., Dai, J. L., Volonteri, M., et al. 2021, MNRAS, 500, 3944
Pfister, H., Toscani, M., Wong, T. H. T., et al. 2022, MNRAS, 510, 2025
Pfister, H., Volonteri, M., Dai, J. L., & Colpi, M. 2020, MNRAS, 497, 2276
Phinney, E. S. 1989, in IAU Symp. 136, The Center of the Galaxy, ed. M. Morris (Dordrecht: Kluwer), 543
Prole, L. R., Schauer, A. T. P., Clark, P. C., et al. 2023, MNRAS, 520, 2081
Rees, M. J. 1988, Natur, 333, 523
Regős, E., Vinkó, J., & Ziegler, B. L. 2020, ApJ, 894, 94
Ricarte, A., Narayan, R., & Curd, B. 2023, ApJL, 954, L22
Rickard, M. J., & Pauli, D. 2023, A&A, 674, A56
Roth, N., Kasen, D., Guillochon, J., & Ramirez-Ruiz, E. 2016, ApJ, 827, 3
Roth, N., Rossi, E. M., Krolik, J., et al. 2020, SSRv, 216, 114
Rydberg, C.-E., Zackrisson, E., Lundqvist, P., & Scott, P. 2013, MNRAS, 429, 3658
Saad, C. R., Bromm, V., & El Eid, M. 2022, MNRAS, 516, 3130
Sadowski, A., & Narayan, R. 2016, MNRAS, 456, 3929
Saha, P., Sluse, D., Wagner, J., & Williams, L. L. R. 2024, SSRv, 220, 12
Saxton, R., Komossa, S., Auchettl, K., & Jonker, P. G. 2020, SSRv, 216, 85
Scannapieco, E., Schneider, R., & Ferrara, A. 2003, ApJ, 589, 35
Schaerer, D. 2003, A&A, 397, 527
Schauer, A. T. P., Bromm, V., Drory, N., & Boylan-Kolchin, M. 2022, ApJL, 934, L6
Schneider, R., Ferrara, A., Natarajan, P., & Omukai, K. 2002, ApJ, 571, 30
Shiokawa, H., Krolik, J. H., Cheng, R. M., Piran, T., & Noble, S. C. 2015, ApJ, 804, 85
Sokasian, A., Yoshida, N., Abel, T., Hernquist, L., & Springel, V. 2004, MNRAS, 350, 47
Spergel, D., Gehrels, N., Baltay, C., et al. 2015, arXiv:1503.03757
Stone, N. C., & Metzger, B. D. 2016, MNRAS, 455, 859
Strubbe, L. E., & Quataert, E. 2009, MNRAS, 400, 2070
Szekerczes, K., Ryu, T., Suyu, S. H., et al. 2024, arXiv:2402.03443
Thomsen, L. L., Kwan, T. M., Dai, L., et al. 2022, ApJL, 937, L28
Trinca, A., Schneider, R., Valiante, R., et al. 2022, MNRAS, 511, 616
van Velzen, S., Gezari, S., Hammerstein, E., et al. 2021, ApJ, 908, 4
Vanzella, E., Meneghetti, M., Caminha, G. B., et al. 2020, MNRAS, 494, L81
Vikaeus, A., Whalen, D. J., & Zackrisson, E. 2022a, ApJL, 933, L8
Vikaeus, A., Zackrisson, E., Schaerer, D., et al. 2022b, MNRAS, 512, 3030
Wang, F., Yang, J., Hennawi, J. F., et al. 2023, ApJL, 951, L4
Wang, J., & Merritt, D. 2004, ApJ, 600, 149
Wang, X., Cheng, C., Ge, J., et al. 2022a, arXiv:2212.04476
Wang, Y., Zhai, Z., Alavi, A., et al. 2022b, ApJ, 928, 1
Welch, B., Coe, D., Diego, J. M., et al. 2022, Natur, 603, 815
Wise, J. H., Turk, M. J., Norman, M. L., & Abel, T. 2012, ApJ, 745, 50
Yajima, H., Abe, M., Fukushima, H., et al. 2023, MNRAS, 525, 4832
Yang, J., Wang, F., Fan, X., et al. 2023, ApJL, 951, L5
Yoshida, N., Bromm, V., & Hernquist, L. 2004, ApJ, 605, 579
Yoshida, N., Omukai, K., Hernquist, L., & Abel, T. 2006, ApJ, 652, 6
Zanazzi, J. J., & Ogilvie, G. I. 2020, MNRAS, 499, 5562
Zhong, S., Li, S., Berczik, P., & Spurzem, R. 2022, ApJ, 933, 96